RESEARCH

Purinergic Signalling Mediates Aberrant Excitability of Developing Neuronal Circuits in the *Fmr1* Knockout Mouse Model

Kathryn E. Reynolds[1] · Eileen Huang[1] · Monica Sabbineni[1] · Eliza Wiseman[1] · Nadeem Murtaza[2] · Desmond Ahuja[3] · Matt Napier[1,5] · Kathryn M. Murphy[3] · Karun K. Singh[4] · Angela L. Scott[1,5]

Abstract

Neuronal hyperexcitability within developing cortical circuits is a common characteristic of several heritable neurodevelopmental disorders, including Fragile X Syndrome (FXS), intellectual disability and autism spectrum disorders (ASD). While this aberrant circuitry is typically studied from a neuron-centric perspective, glial cells secrete soluble factors that regulate both neurite extension and synaptogenesis during development. The nucleotide-mediated purinergic signalling system is particularly instrumental in facilitating these effects. We recently reported that within a FXS animal model, the *Fmr1* KO mouse, the purinergic signalling system is upregulated in cortical astrocytes leading to altered secretion of synaptogenic and plasticity-related proteins. In this study, we examined whether elevated astrocyte purinergic signalling also impacts neuronal morphology and connectivity of *Fmr1* KO cortical neurons. Here, we found that conditioned media from primary *Fmr1* KO astrocytes was sufficient to enhance neurite extension and complexity of both wildtype and *Fmr1* KO neurons to a similar degree as UTP-mediated outgrowth. Significantly enhanced firing was also observed in *Fmr1* KO neuron-astrocyte co-cultures grown on microelectrode arrays but was associated with large deficits in firing synchrony. The selective $P2Y_2$ purinergic receptor antagonist AR-C 118925XX effectively normalized much of the aberrant *Fmr1* KO activity, designating $P2Y_2$ as a potential therapeutic target in FXS. These results not only demonstrate the importance of astrocyte soluble factors in the development of neural circuitry, but also show that P2Y purinergic receptors play a distinct role in pathological FXS neuronal activity.

Keywords Astrocytes · Neuronal development · Purinergic signalling · Fragile X Syndrome · Uridine triphosphate · Microelectrode arrays

Introduction

During development, the formation of appropriate neuronal connections is heavily dependent on the intricate choreography of neuronal and glial interactions. Astrocytes are highly prevalent CNS glial cells and key participants of these early neurodevelopmental processes. It is therefore not surprising that defects to normal astrocyte function have been associated with several neurodevelopmental diseases, including autism spectrum disorders (ASDs). Specifically, astrocyte dysfunction has been primarily demonstrated in monogenic ASDs caused by single gene mutations, such as the CGG repeat expansion of the *Fmr1* gene in Fragile X Syndrome (FXS). The mutation to *Fmr1* in FXS leads to the deletion of RNA-binding protein FMRP and subsequently abnormal creation, refinement, and excitation of neurological networks that underlie seizures and sensory hyperresponsivity

✉ Angela L. Scott
  angela.scott@uoguelph.ca

1   Department of Pathology and Molecular Medicine, McMaster University, Hamilton, ON, Canada

2   McMaster Stem Cell and Cancer Research Institute, McMaster University, Hamilton, ON, Canada

3   Department of Psychology, Neuroscience, and Behaviour, McMaster University, Hamilton, ON, Canada

4   University Health Network, Toronto, ON, Canada

5   Department of Molecular and Cellular Biology, University of Guelph, 488 Gordon St, Guelph, ON, Canada

[1–8]. Astrocyte-specific deletion of FMRP is sufficient to produce abnormal neuronal morphology in vitro and alter mouse motor neuron morphology and motor skill acquisition in vivo [9, 10]. Identifying the astrocyte-mediated factors that lead to aberrant cortical circuitry in early postnatal development will provide important insight into the molecular and cellular pathology of FXS, ASDs, and related neurodevelopmental disorders.

Astrocytic regulation of the neuronal microenvironment is modulated through a variety of molecular families, including the purinergic signalling system. Purines, pyrimidines, and their metabolites (ex. ATP, UTP, ADP, etc.) signal within the CNS via several receptor families, including P2Y, P2X and P1 receptors [reviewed in 11]. Recently, our work has shown that several P2Y receptors are significantly upregulated in cortical astrocytes of the *Fmr1* knockout (KO) mouse model of FXS [12]. Both neurons and astrocytes express the excitatory G_q-coupled P2Y family of purinergic receptors that are activated by the nucleoside di- and triphosphates ATP, ADP, UTP, and UDP. P2Y activation initiates phospholipase C-inositol triphosphate-mediated calcium release pathways, and promotes propagation of astrocyte intercellular calcium waves, vesicular release of purinergic neuro/gliotransmitters, and changes in gene expression [11]. Specifically, $P2Y_2$ and $P2Y_6$ receptor expression is elevated in *Fmr1* KO mouse cortical astrocytes, and activation via ATP or UTP enhances both calcium mobilization and secretion of the pro-synaptogenic factor thrombospondin-1 (TSP-1) [12–14]. However, how purinergic signalling aberrations in *Fmr1* KO astrocytes during early postnatal development contributes to FXS neuronal morphology and network function remains unclear.

In this study, we investigated the role of astrocyte purinergic signalling dysregulation in FXS on the development of cortical neurons. Previous work has shown that neurons isolated from the brain of *Fmr1* KO mice display aberrant neurite outgrowth, extensive arborization, an excess of immature dendritic spines, and increased synaptic puncta [10, 15, 16]. These structural phenotypes are correlated with heightened neuronal excitation and deficits in inhibitory activity, a combination also reflected in many individuals with ASD [7, 17, 18]. Here, we found that FMRP expression in astrocytes was the primary determining factor of neurite outgrowth, and astrocyte-conditioned media (ACM) from *Fmr1* KO astrocytes was sufficient to induce an FXS-like neuronal phenotype of enhanced neurite outgrowth in wildtype (WT) cortical neurons. The promotion of growth of WT cortical neurons was mirrored by the application of exogenous UTP in the presence of WT ACM, but not *Fmr1* KO ACM. In addition, elevated firing of *Fmr1* KO mouse cortical neurons co-cultured with astrocytes was normalized following chronic $P2Y_2$ antagonism. Our findings not only emphasize the importance of astrocyte-derived signals in FXS neuronal pathophysiology, but also highlight the potential of $P2Y_2$ inhibition as a therapeutic strategy for FXS and ASDs.

Methods

Animals

Two genotypes of mice, wildtype (WT) and *Fmr1*$^{-/-}$*(Fmr1* KO; FVB.129P2(B6)-Fmr1^{tm1Cgr}), were bred and housed at the McMaster Health Sciences Central Animal Facility. All mouse housing conditions and experimental protocols were authorized by the McMaster Animal Ethics Board (Animal Utilization Protocol 21-02-06), following Canadian Council on Animal Care policies. Timed pregnant dams were removed for brain dissection and neuronal isolation once embryos reached approximately embryonic day (E) 16, while pups of both sexes were removed at postnatal day (P) 1–3 for astrocyte dissection.

Primary Astrocyte Culture

Cortices from three P1-3 WT or *Fmr1* KO mouse pups, euthanized by decapitation, were pooled to obtain each primary astrocyte culture. Following protocols previously described [19], whole brains were placed into ice-cold calcium- and magnesium-free Hanks' buffered saline solution (CMF-HBSS; Invitrogen, Waltham, MA, USA). Using a Zeiss Stemi SR stereo microscope (Carl Zeiss, Oberkochen, Germany), olfactory bulbs, meninges, and hippocampi were detached to isolate both hemispheres of the cerebral cortex. Cortical hemispheres were dissociated in 1 mg/mL DNase (Roche Applied Science) and 0.25% trypsin (Invitrogen), then seeded in glial-selective media (minimum essential media (Gibco, Waltham, MA, USA), 10% horse serum (Gibco), and 0.6% D-(+)-glucose (Sigma-Aldrich, St. Louis, MO, USA). Primary astrocyte cultures were grown within a humidified incubator (37ºC, 5% CO_2; NuAire, Plymouth, MN, USA) for a total of 6–8 days in vitro (DIV), with 50% media changes 24 h post-plating and every subsequent 48–72 h.

Once cultures achieved 75–90% confluence, they were utilized to produce astrocyte-conditioned media (ACM) or replated on top of neurons within microelectrode arrays (see Microelectrode Arrays). To produce ACM, glial-selective media was replaced with neuronal maintenance media (NMM) containing NeuroCult Basal Medium (StemCell Technologies, Vancouver, ON, Canada), 2% SM1 neuronal supplement (StemCell Technologies), 0.1125% Glutamax (Invitrogen), and 0.1% glutamine (Invitrogen). Astrocyte

cultures were maintained at 37ºC and 5% CO_2 for an additional 48 h to allow for the accumulation of astrocyte-secreted factors within the media.

Primary Neuron Culture

Timed pregnant WT and *Fmr1* KO dams were euthanized by CO_2 overdose once embryos reached ~E16. Following abdominal sterilization with 95% ethanol, uterine horns were removed through a midline incision through the skin and abdominal wall, then rinsed in sterile ice-cold CMF-HBSS (Invitrogen). Three embryos from each litter were randomly selected for dissection. Skin, skull, olfactory bulbs, meninges, and hippocampi were removed from one cortical hemisphere per embryo under a Zeiss Stemi SR stereo microscope (Carl Zeiss). Cortical tissue was dissociated in CMF-HBSS plus 0.25% trypsin, using a series of mechanical dissociation steps outlined previously [19]. Neurons intended for neurite outgrowth and Sholl analyses were then resuspended in ACM and plated on 1 mg/mL poly-L-lysine (Sigma-Aldrich) and 10 μg/mL laminin (Invitrogen)-coated 12 mm coverslips (Neuvitro, Vancouver, WA), at a density of 7000 cells/coverslip.

The two different genotypes of neurons and ACM (WT and *Fmr1* KO) were combined to create four separate groups: WT neurons cultured with WT ACM (WTN-WTACM), WT neurons cultured with *Fmr1* KO ACM (WTN-KOACM), *Fmr1* KO neurons cultured with WT ACM (KON-WTACM), and *Fmr1* KO neurons cultured with *Fmr1* KO ACM (KON-KOACM). Each combination was plated in duplicate, and cultured four times using separate litters, for a total of eight coverslips (n) per combination. Neurons were treated 24 h and 72 h after plating with one of the following concentrations of UTP (diluted in PBS; ThermoFisher): 0.1 μM 1 μM, 10 μM, or 100 μM, or phosphate buffered saline control (PBS; Life Technologies). Primary neuron cultures were maintained at 37ºC and 5% CO_2 for a total of 5DIV, without media changes. Survival of neurons within each condition was high (~95%) and equivalent across all treatment groups.

Immunocytochemistry

Primary neuron cultures and neuron-astrocyte co-cultures were processed for immunocytochemistry using protocols previously described [20]. Briefly, neurons cultured in ACM were fixed in 100% ice-cold acetone (BioShop, Burlington, ON) at 5DIV for analysis, while co-cultures were fixed at 7DIV for representative imaging. Fixed cells were permeabilized with 0.1% Triton X-100 (BDH Chemicals, Radnor, PA, USA) and blocked with 1% bovine serum albumin (BSA; Sigma-Aldrich). Neurons were incubated

in anti-MAP2 primary antibody (mouse monoclonal; 1:250 in PBS; Invitrogen Cat# 13-1500, RRID: AB_2533001) overnight at 4ºC, then in goat anti-mouse fluorescein isothiocyanate (FITC) (1:100 in PBS; Jackson ImmunoResearch, West Grove, PA, USA Cat# 115-095-166, RRID: AB_2338601) secondary antibody for 3 h at room temperature. Co-cultures were also incubated in anti-MAP2 primary antibody as well as anti-glial fibrillary acidic primary antibody (GFAP; chicken polyclonal; 1:1000; OriGene, Rockville, MD, USA Cat# TA309150), followed by donkey anti-mouse AlexaFluor 594 (1:500; Invitrogen Cat# 21203, RRID: AB_141633) and donkey anti-chicken FITC (1:100; Jackson ImmunoResearch Cat# 703-095-155, RRID: AB_2340356) secondary antibodies. Prolong Gold anti-fade mounting medium plus 4',6-diamidino-2-phenylindole (DAPI; Invitrogen) was used to stain nuclei with DAPI and affix the coverslips onto slides. Neurons were imaged by a blinded experimenter at x20 objective magnification, using a Zeiss Axio Imager.M2 epifluorescent microscope (Carl Zeiss) fitted with an Axiocam 506 camera (Carl Zeiss) and ZEN Blue acquisition software (Carl Zeiss).

Neurite Outgrowth and Sholl Analysis

Neurite outgrowth and complexity in UTP-treated neurons were simultaneously assessed using Fiji software (ImageJ; National Institutes of Health, Bethesda, MD, USA). All analyses were performed by experimenters who were blinded to the treatment conditions and hypotheses. Each treatment group consisted of 8 coverslips isolated from embryos of four separate dams ($n = 8$; $n = 6$ for the following groups: WTN-WTACM 10 μM UTP, WTN-KOACM 1 μM UTP, KON-WTACM 10 μM UTP, and KON-KOACM 10 μM UTP). Five images representative of the total neuronal population were taken per coverslip. From those images, ~4 neurons per image were randomly chosen for analysis, for a total of ~20 neurons analyzed per n and ~120–160 neurons analyzed per condition. Each neurite of a selected neuron was traced from proximal to distal end using the Simple Neurite Tracer Fiji plugin, and radius step size was set to 10 μm for Sholl analysis. Traces began outside the soma at the base of each neurite to ensure that the soma was excluded from outgrowth measurements. Results of both neurite outgrowth and Sholl analyses were expressed as fold change relative to PBS control.

Protein Analysis

Cell lysates from WT and *Fmr1* KO mouse primary neuron cultures were prepared for western blotting to compare levels of neuronal P2Y receptors. For $P2Y_1$ quantification, experimental samples consisted of 3 WT ($n = 3$) and

5 *Fmr1* KO ($n=5$) cultures from individual timed pregnancies, while for P2Y$_2$ western blotting, 6 (n) separate neuron cultures per genotype were used. Experimental samples for P2Y$_4$ western blotting were obtained from 4 WT ($n=4$) and 3 *Fmr1* KO ($n=3$) cultures isolated from separate litters, and 5 (n) separate neuron cultures per genotype were used for P2Y$_6$ western blotting. Following dissociation protocols described above (see Primary Neuron Culture), neurons were plated on 1 mg/mL PLL- and 10 µg/mL laminin-coated 6-well plates (Corning, NY, USA) and maintained for 5DIV, then lifted using 0.05% trypsin-ethylenediaminetetraacetic acid (trypsin-EDTA; Gibco). Following centrifugation and removal of supernatant, pelleted cultured neurons were flash frozen in liquid nitrogen and stored at -80 °C until homogenization with RIPA lysis buffer (150 mM NaCl, 1% NP-40, 0.5% deoxycholic acid, 1% SDS, 50 mM Tris, Roche ULTRA protease inhibitor, Roche PhoSTOP phosphatase inhibitor), as previously described [21]. Total protein levels within each lysate were quantified using a DC protein assay (BioRad, Mississauga, ON, Canada) to determine gel loading dilutions.

Western blotting samples were comprised of 5 µg protein lysate per lane, diluted in Laemmli sample buffer plus 2.5% ß-mercaptoethanol (BioRad). Following gel electrophoresis using polyacrylamide TGX 4–12% gradient gels (BioRad), proteins were transferred to polyvinylidene difluoride (PVDF) (BioRad) membranes, which were then agitated in a blocking solution of 5% non-fat milk in 1X Tris-buffered saline solution with Tween-20 (TBS-T). Membranes were incubated overnight at 4°C with primary antibodies against the following P2Y receptors: P2Y$_1$ (rabbit polyclonal; 1:200; Alomone Labs, Jerusalem, Israel Cat# APR-009, RRID: AB_2040070; band at $\sim$66 kDa) [22], P2Y$_2$ (rabbit polyclonal; 1:200; Alomone Labs Cat# APR-010, RRID: AB_2040078; band at $\sim$47 kDa [22], P2Y$_4$ (rabbit polyclonal; 1:200; Alomone Labs Cat# APR-006, RRID: AB_2040080; band at $\sim$50 kDa) [23, 24], and P2Y$_6$ (rabbit polyclonal; 1:200; Alomone Labs Cat# APR-106, RRID: AB_2040082; band at $\sim$65 kDa) [23, 25]. Membranes were subsequently incubated in donkey-anti rabbit horseradish peroxidase secondary antibody (1:2500; GE Healthcare Cat# NA934) for 2 h, then developed in Clarity MAX enhanced chemiluminescence (ECL) substrate (BioRad) and imaged using a ChemiDoc imaging system (BioRad). Following development, membranes were stripped using Blot Restore Solution (MilliporeSigma) and re-probed with ß-actin primary antibody (mouse monoclonal; 1:5000; MilliporeSigma Cat# A5441, RRID: AB_476744) and donkey-anti mouse horseradish peroxidase secondary antibody (1:2500; GE Healthcare Cat# NA931V) to serve as a loading control. Bands of interest were quantified and normalized to ß-actin using ImageLab 6.0.1 software (BioRad).

P2Y receptor levels were expressed as fold change relative to WT means.

Neuron-Astrocyte Co-Cultures

WT and *Fmr1* KO neurons intended for co-culture on microelectrode arrays were dissected according to protocols described above (see Primary Neuron Culture), then resuspended in NeuroCult Neuronal Plating Medium (NMM, STEMCELL Technologies, Vancouver, BC, Canada) supplemented with 2% STEMCELL Modified-1 Neuronal Supplement (SM1, STEMCELL Technologies). Neurons were seeded at a density of 30,000 cells per well on Axion 48-well Cytoview plates (Axion Biosystems, Atlanta, GA, USA) containing 16 microelectrodes per well with a 0.32 cm^2 total recording electrode area, pre-coated with 0.1% polyethylenimine (PEI) in borate buffer (pH 8.4). After 24 h, confluent astrocytes of the same genotype (see Primary Astrocyte Culture) were added to the culture at a density of 60,000 cells per well. On-plate reservoirs were filled with 5–7 mL of sterile water to increase humidity and to prevent evaporation of cell suspensions and media. Co-cultures were maintained in a humidified incubator at 37 °C and 5% CO$_2$, with media changes 2x per week and >24 h prior to recording, as media changes temporarily dysregulate neuronal firing. Between 5-11DIV, cells received half media changes consisting of BrainPhys Neuronal Medium (STEMCELL Technologies, Vancouver, BC, Canada) supplemented with 2% SM1. Starting at 12DIV, half media changes consisted of BrainPhys Neuronal Medium with 2% SM1 and 7.5 mM glucose.

Microelectrode Array Recording and Analysis

Neuronal firing activity was recorded every 2–3 days, from 7-35DIV, using the Axion MaestroPro multi-well plate recording system (Axion Biosystems) set to detect spontaneous real-time neural spikes. All recordings were carried out for 10 min at a temperature of 37 °C, in the absence of CO$_2$ regulation. Wells with less than 9 of the 16 total electrodes (<50%) detecting neuronal activity, defined as a minimum spike rate of 5 spikes per minute, were removed prior to data analysis unless they recovered to $\geq 9/16$ active electrodes in subsequent recordings.

P2Y antagonist treatments were applied to culture media 2x per week and >24 h prior to recording, starting at 5DIV and continuing until 31DIV. Cultures were treated with either the specific P2Y$_2$ antagonist AR-C 118925XX (AR-C; 1 µM and 10 µM in 50% PBS/50% DMSO; Tocris Bioscience, Bristol, UK) or the general P2 antagonist suramin (0.1 µM in 50% PBS/50% DMSO; Tocris Bioscience). Some cultures were unable to be recorded for the full

experimental period due to external factors. The WT naïve experimental group consisted of a total of 13 culture samples ($n = 13$) obtained from 7 individual timed pregnancies, with 6 cultures remaining at 35DIV, while the *Fmr1* KO naïve experimental group was comprised of 15 culture samples ($n = 15$) from 6 separate dams and was reduced to 8 cultures by 35DIV. The WT AR-C 118925XX (1 μM) experimental group was composed of 14 culture samples ($n = 14$) at 7DIV and 8 cultures at 35DIV. Fourteen WT cultures ($n = 14$) at 7DIV and 7 WT cultures by 35DIV were treated with 10 μM antagonist, each derived from 7 individual timed pregnancies. *Fmr1* KO 1 μM AR-C 118925XX samples consisted of 12 cultures ($n = 12$) at 7DIV and 3 cultures at 31DIV obtained from 7 individual dams; while *Fmr1* KO 10 μM samples were made up of 11 cultures ($n = 11$) at 7DIV and 7 cultures at 35DIV obtained from 6 individual dams. Suramin experimental samples were composed of 10 WT culture samples ($n = 10$) at 7DIV and reduced to 8 cultures by 35DIV, as well as 9 *Fmr1* KO culture samples ($n = 9$) at 7DIV and 5 wells at 35DIV, each obtained from 5 individual timed pregnancies per genotype.

A reversible treatment of AMPA and NMDA receptor blockers, CNQX and AP-5 (10 μM; MilliporeSigma, Oakville, ON, CA), was applied at 7DIV, 10DIV and 12DIV to ensure that recordings detected synaptic firing and not gap junction activity. Combined CNQX + AP-5 treatments were applied to separate samples (WT $n = 14$ from 7 separate timed pregnancies; *Fmr1* KO $n = 12$ from 6 individual timed pregnancies) for a 10 min incubation period plus 10 min recording time, then the culture media was removed and replaced in order to restore neuronal firing. All analysis of firing activity was completed using AxIS Metric software (Axion Biosystems) with default settings applied for neural spike, burst, and network burst parameters. Relevant measured metrics, processed by the Neural Statistics Compiler (Axion), are defined in Table 1.

Statistical Analysis

GraphPad Prism 9.1.0 software (GraphPad Software, San Diego, CA, USA) was used for all graphing and statistical analyses. Neuronal outgrowth and complexity analyses between three or more means within a single genotype were performed by fitting the data to a mixed model followed by post-hoc Sidak multiple comparisons tests; the mixed model was chosen in place of a one-way repeated measures analysis of variance (ANOVA) due to missing replicates in 10 μM UTP conditions. Comparisons between three or more means across different genotypes were performed using two-way or three-way ANOVA with post-hoc Sidak corrections. All statistical results were considered significant at $p < 0.05$, and reported statistics are adjusted p values

obtained from post-hoc Sidak corrections unless otherwise specified. Western blotting comparisons, made between two means, were performed using two-tailed, unpaired t-tests with significance at $p < 0.05$. All data is presented as means +/- SEM.

Time series comparisons of MEA metrics between WT and *Fmr1* KO naïve groups were performed using mixed models, chosen in place of two-way repeated measures ANOVA due to missing values at later time points, as some cultures were unable to be followed for the full 35DIV due to external factors. Differences between WT and *Fmr1* KO treatment groups over time were initially analyzed using three-way ANOVA, then parameters of interest at select time points were further compared between genotypes and treatments using two-way ANOVA followed by post-hoc Holm-Sidak multiple comparisons tests. All line graphs present data as means +/- SEM, while box plots present the median and interquartile range with whiskers extending to minimum and maximum values. All statistical comparisons were considered significant at $p < 0.05$.

High-Dimensional Clustering Analysis

A cluster analysis was completed in RStudio (Boston, MA) to identify whether samples (n) at the biologically relevant timeframe of 28DIV formed groups in high-dimensional space. Subsets of data from each genotype ($n_{WT} = 30$, $n_{KO} = 24$) originated from 23 MEA metrics, or features of interest (p), outlined in Table 1. Data in each subset were z-scored according to treatment group and subsequently arranged in an n x p feature matrix; if needed, values were imputed using the *impute.knn* function from the *impute* package (version 1.64.0). Data sets were then clustered using the Robust Sparse K-means Clustering (RSKC) algorithm implemented in the *RSKC* package (version 2.4.2) [26]. Sparse clustering algorithms utilized here have been successfully used to study molecular brain development, where $p \approx n$ [27].

Each data set underwent 100 iterations of RSKC for values of K ranging from 2 to 3 clusters, ensuring that a minimum of three samples were assigned per cluster. Across every iteration, the cluster assignments for each sample and the RSKC weights for each feature were saved. The optimal number of clusters was determined with an adapted elbow method. Briefly, using the *KMeansSparseCluster* function from the *sparcl* package (version 1.0.4), the average within-cluster sums of squares (WCSS) was found for each value of K across 100 iterations. The elbow was identified using the *elbowPoint* function of the *akmedoids* package (version 0.1.5). This approach found the optimal number of clusters for the WT and *Fmr1* KO data sets to be $K = 6$ and $K = 5$, respectively. Then, the most representative of the 100 iterations were then determined by averaging

Table 1 Parameters used to define microelectrode array (MEA) metrics. Adapted from Axion Biosystems (2017)

MEA Metric	Abbreviation	Definition
Spike		A change in voltage measured by an MEA electrode, exceeding the background signal by an adaptive threshold of ≥ 6 x standard deviations. Spikes are presumed action potentials.
Active Electrode		Any electrode detecting a minimum spike rate of 5 spikes per minute throughout the recording period. Only wells with $\geq 9/16$ ($> 50\%$) active electrodes were analyzed.
Mean Firing Rate	MFR	Total number of spikes detected across all 16 electrodes within the MEA well $\div$ total recording time (10 min). Units: Hz
Weighted Mean Firing Rate	WMFR	Mean firing rate adjusted for the total number of active electrodes within the well. Units: Hz
Burst		A group of ≥ 5 spikes detected by a single active electrode. Consecutive spikes must occur within a 100 ms interval.
Burst Frequency	BF	Total number of bursts detected $\div$ total recording time (10 min). Units: Hz
Burst Duration	BD	Average length of burst, from first spike to last spike. Units: s
Number of Spikes per Burst	NOSPB	Average number of spikes recorded from a single electrode during a burst.
Number of Bursting Electrodes	NOBE	Number of electrodes detecting bursts within a single well.
Burst Percentage	BP	Percentage of spikes that are associated with a bursting event. Units: %
Inter-Spike Interval	II	Average length of time between spikes. Units: s
Inter-Spike Interval within Burst	ISIWB	Average length of time between spikes that occur within a single burst. Units: s
Inter-Spike Interval Coefficient of Variation	ISICOV	Inter-spike interval standard deviation $\div$ mean. Values > 1 indicate bursting activity.
Inter-Burst Interval	IBI	Time between the onset of bursts. Units: s
Inter-Burst Interval Coefficient of Variation	IBICOV	Inter-burst interval standard deviation $\div$ mean. Unitless. Small values indicate regularly occurring bursts.
Normalized Duration Interquartile Range	NDIQR	Regularity of the time between single-electrode bursts. Unitless. Small values indicate consistent burst durations.
Network Burst		≥ 50 spikes detected by $\geq 6/16$ active electrodes within a well, within a synchrony window of 20 ms. Consecutive spikes must occur within a 100 ms interval.
Network Burst Frequency	NBF	Total number of network bursts detected $\div$ total recording time (10 min). Units: Hz
Network Burst Duration	NBD	Average length of network burst, from first spike to last spike. Units: s
Number of Spikes per Network Burst	NOSPNB	Number of spikes detected by all participating electrodes (recording ≥ 5 spikes/min) within a network bursting event.
Network Burst Percentage	NBP	Percentage of spikes that are associated with a network burst. Units: %
Number of Electrodes Participating in Network Burst	NEPINB	Number of electrodes recording ≥ 5 spikes/min during a network burst. High values indicate high levels of culture-wide network connectivity.
Number of Spikes per Network Burst per Channel	NOSPNBPC	Average number of spikes recorded during a network burst $\div$ number of electrodes detecting network burst activity.
Network Inter-Burst Interval Coefficient of Variation	NIBICOV	Inter-network burst interval standard deviation $\div$ mean. Unitless. Unitless. Small values indicate regularly occurring network bursts.
Network Normalized Duration Interquartile Range	NNDIQR	Regularity of the time between network bursts. Small values indicate consistent network burst durations.
Synchrony Index	SI	Probability that a neuronal spike recorded by one electrode is temporally related to a spike detected by a different electrode. Unitless. Values close to 1 indicate that neurons at distinct electrodes fire together with high synchrony. Computed by finding the cross-correlation of spike pairs within the well.
Area Under Normalized Cross-Correlation	AUNCC	Area under the cross-correlogram curve used to compute synchrony index, adjusted for spike regularity. Unitless. High AUNCC values indicate high synchronicity of firing.
Width at Half Height of Normalized Cross-Correlation	WAHHONCC	Half width of the cross-correlogram curve used to compute synchrony index, adjusted for spike regularity. Unitless. Narrow WAHHONCC widths indicate high synchrony across the network.

the feature weights across all iterations for a given *K*, thus yielding a vector of 23 mean weights. For each iteration, the mean squared error (MSE) was calculated using its feature weights. Due to the sample size of the data, two additional constraints were applied to ensure biologically interpretable results: each cluster must have no less than three samples,

and the most representative iteration must be chosen from the top five ranked iterations (those with the smallest MSE). Once determined, pie charts were constructed for each treatment to illustrate clusters, while bar graphs grouped related features together (average and SEM). To visualize the high-dimensional relationships between samples,

dimensionality-reduction was done using the t-distributed stochastic neighbour embedding (t-SNE) algorithm implemented in the *Rtsne* package (version 0.15) [28]. Each column in the n x p feature matrix was multiplied by its corresponding RSKC weight from the most representative iteration to enhance the signal in clustering variables, while reducing the impact of noise variables and accurately capturing the global pattern of a high-dimensional data sets [29, 30]. The output of t-SNE was then visualized on a two-dimensional scatter plot. Each point on the scatter plot was colour-coded and shaped according to its experimental treatment, and points that were assigned to the same cluster were enveloped in coloured ellipses.

Results

UTP Increases Neurite Outgrowth of WT and *Fmr1* KO Neurons in only WT Conditions

To isolate the effect of neuronal vs. astrocyte soluble factors, WT and *Fmr1* KO neurons (WTN and KON) were cultured with either WT or *Fmr1* KO astrocyte-conditioned media (WTACM or KOACM) to form four distinct culture conditions, as shown in Fig. 1A. WT neurons grown in WTACM and treated with high-dose UTP (10 μM, $n = 6$ and 100 μM, $n = 8$) for 5DIV (Fig. 1B-D) displayed an increase in maximal neurite extension (i.e., the length of the neuron's longest neurite) relative to PBS control treatment (10 μM, $p = 0.0285$ and 100 μM, $p = 0.0258$). However, incubation with lower concentrations of UTP (0.1 μM and 1 μM, $n = 8$) did not influence neurite length (0.1 μM, $p = 0.1951$ and 1 μM, $p = 0.3366$). Surprisingly, a robust effect of UTP was also observed with *Fmr1* KO neurons grown in WTACM (Fig. 1E). Within this condition, sustained treatment with both high and lower concentrations of exogenous UTP significantly elevated maximal neurite extension above PBS (0.1 μM UTP, $p = 0.0521$; $n = 8$; 1 μM UTP, $p = 0.0054$, $n = 8$; 10 μM UTP, $p = 0.0084$, $n = 6$; and 100 μM UTP, $p = 0.0096$, $n = 8$). In contrast, we did not observe any changes to maximal neurite extension when neurons of either genotype were grown in *Fmr1* KO ACM. For WT neurons grown in *Fmr1* KOACM (Fig. 1F), neither low-dose UTP (0.1 μM, $p > 0.9999$, $n = 8$ and 1 μM, $p = 0.5652$, $n = 6$) nor high-dose UTP (10 μM, $p = 0.9368$, $n = 8$ and 100 μM, $p = 0.4953$, $n = 8$) impacted the length of the longest neurite relative to PBS treatment ($n = 8$). Similarly, the maximal neurite extension of *Fmr1* KO neurons grown in *Fmr1* KO ACM (Fig. 1G) was unaffected by any of the UTP concentrations we tested (0.1 μM UTP, $p = 0.8606$, $n = 8$; 1 μM UTP, $p = 0.5419$, $n = 8$; 10 μM UTP, $p = 0.9995$, $n = 6$; and 100 μM UTP, $p = 0.9993$, $n = 8$). When we compared

maximal neurite lengths between the PBS controls of our four genotype conditions, neurons grown in WTACM exhibited shorter baseline neurite extension than neurons grown in *Fmr1* KOACM (Fig. 1C). Both PBS-treated WT and *Fmr1* KO neurons grown in *Fmr1* KOACM grew significantly longer neurites than those in the WTN-WTACM condition ($p = 0.0056$ and $p = 0.0040$, respectively, $n = 8$; Fig. 1I, J), while the maximal neurite length of *Fmr1* KO neurons in WTACM did not significantly differ from that of WT neurons in WTACM ($p = 0.2796$, $n = 8$; Fig. 1C, H).

Treatment with 100 μM UTP elevated WT neuron outgrowth in WTACM to levels comparable to PBS controls of *Fmr1* KOACM-grown neurons ($p = 0.9925$ versus KON-KOACM, Fig. 1C, J; $p = 0.9811$ versus WTN-KOACM, Fig. 1C, I). When *Fmr1* KO neurons were grown in WTACM, the maximal neurite length was also significantly longer than that of UTP-treated WTN-WTACM ($p = 0.0125$; Fig. 1H). Notably, additional growth with exogenous UTP treatment was not observed in either genotype of neurons grown with *Fmr1* KOACM (WTN-KOACM, $p = 0.2131$, Fig. 1I and KON-KOACM, $p = 0.9842$, Fig. 1J).

UTP Increases Complexity of Cortical Neurons Grown with Wildtype Astrocytes only

To determine the influence of UTP on neurite branching and complexity in neurons 5DIV, we used a Sholl analysis to record the number of neurites that intersected concentric circles radiating from the centre of the neuronal soma. The pattern of Sholl intersections was similar across all conditions: the number of intersections rose sharply at radii 20 μm from the neuron soma, then declined with increasing distance from the soma, reaching a plateau between ~ 80–120 μm radii (Fig. 2B, C). For control groups treated with only PBS, no combination of culture condition significantly differed from that of WTN-WTACM (versus KON-WTACM $p = 0.7449$; WTN-KOACM $p = 0.0670$; KON-KOACM $p = 0.7509$; Fig. 2H).

For WT neurons grown in WTACM, we found that UTP did indeed influence neurite complexity: 10 μM and 100 μM UTP treatments led to an increase in the total number of Sholl intersections relative to PBS control (10 μM UTP $p = 0.0115$, $n = 6$ and 100 μM UTP $p = 0.0172$, $n = 8$), but not 0.1 μM or 1 μM UTP ($p = 0.5939$ and $p = 0.1179$ respectfully; $n = 8$) (Fig. 2B, D). The purinergic-mediated increase in WTN-WTACM arborization, with 10 μM UTP for example, is broadly distributed throughout each Sholl radius, with significant effects of treatment (ℰ; $p = 0.0006$), genotype (*; $p < 0.0001$) and Sholl radius (δ; $p < 0.0001$), as well as significant interactions of genotype x radius (σ; $p = 0.0188$) and genotype x treatment (ω; $p < 0.0001$) (Fig. 2C). *Fmr1* KO neurons grown in WTACM also increased branching
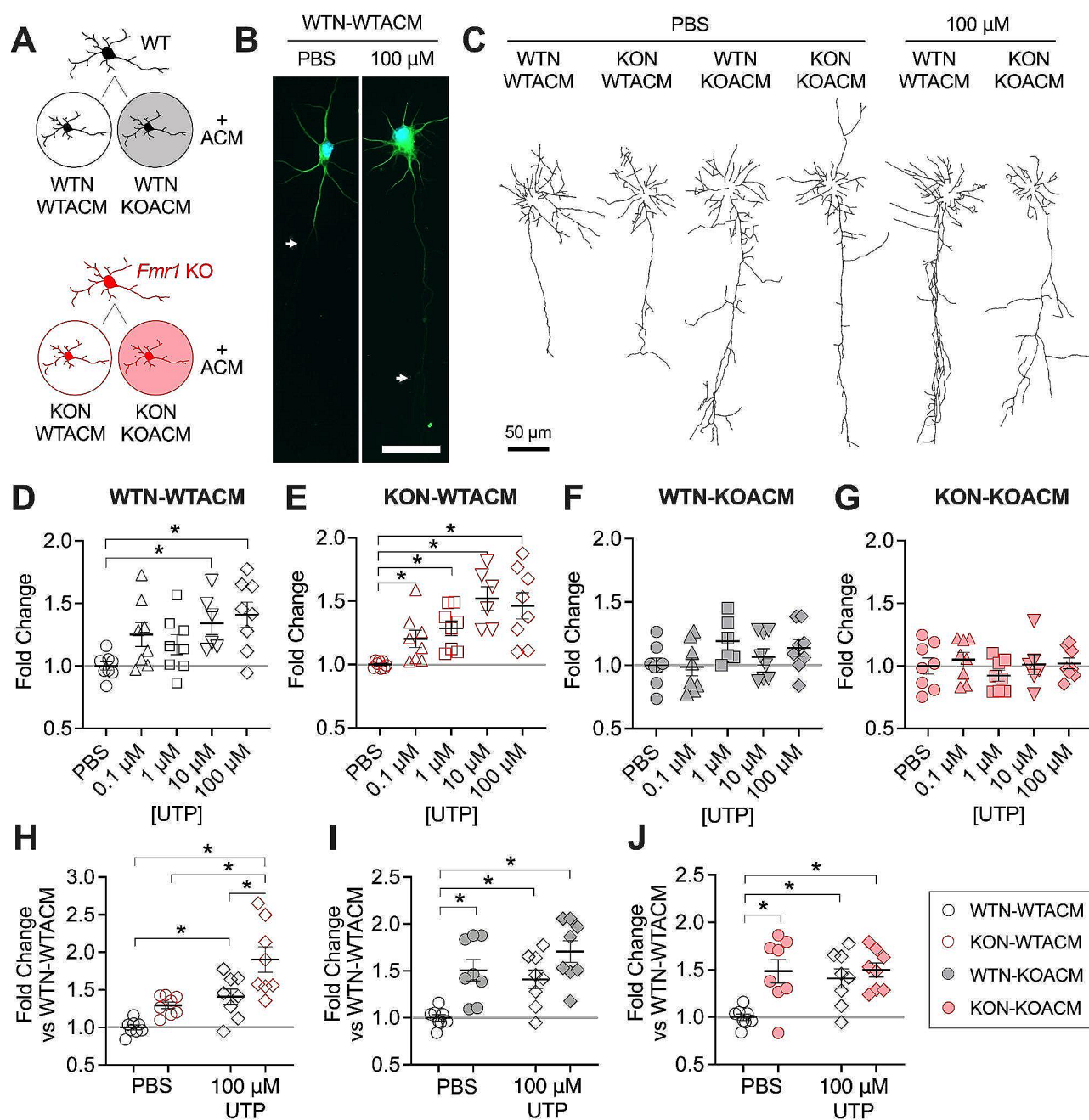
Fig. 1 Extension of the longest neurite in WT and *Fmr1* KO primary neurons cultured for 5DIV with either WT or *Fmr1* KO astrocyte-conditioned media and treated with the P2Y agonist UTP (0.1 μM, 1 μM, 10 μM, or 100 μM, or PBS control). **A.** Schematic outlining the four different genotype conditions within neurite outgrowth experiments. **B-C.** Representative immunofluorescence (**B**) and neurite traces (**C**) following PBS and 100 μM UTP treatment. Scale bars: 50 μm. UTP treatment increased the length of the longest neurite (i.e. the putative axon) in (**D**) WTN-WTACM (p ≤ 0.0258) and (**E**) KON-WTACM conditions (p ≤ 0.0054), but not in (**F**) WTN-KOACM or (**G**) KON-KOACM. **H-J.** Between-genotype comparisons of PBS vs. 100 μM UTP in (**H**) KON-WTACM (p ≤ 0.0125), (**I**) WTN-KOACM (p ≤ 0.0056), and (**J**) KON-KOACM groups (p ≤ 0.0040) relative to WTN-WTATCM. All data presented as means +/- SEM, with gray horizontal lines indicating control means. *n*=8, with the exception of *n*=6 for 10 μM WTN-WTACM, KON-WTACM, KON-KOACM, and 1 μM WTN-KOACM. Significant differences between groups denoted by *; *p*<0.05
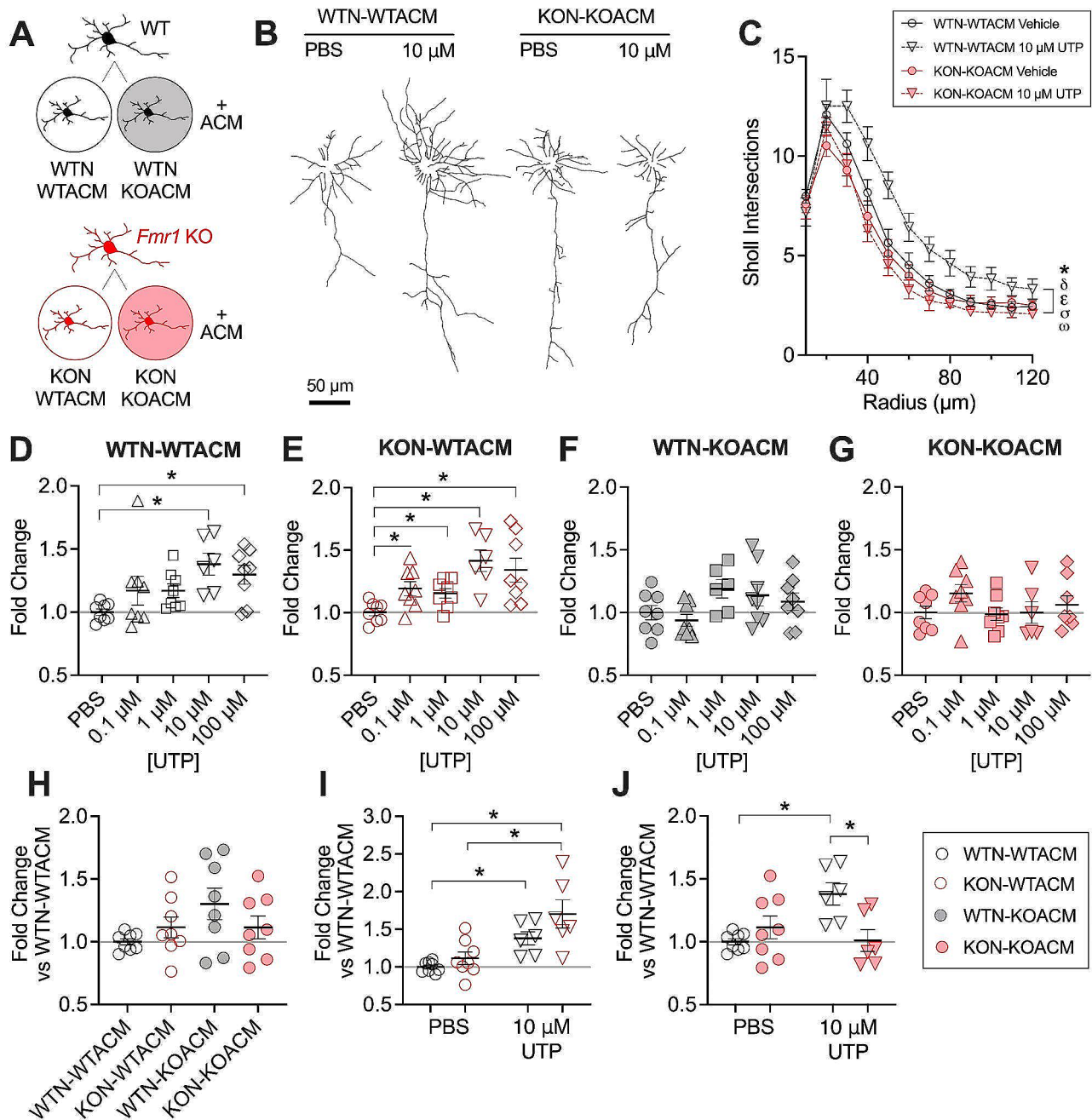
Fig. 2 Sholl analysis of WT and *Fmr1* KO primary neurons cultured with WT or *Fmr1* KO astrocyte-conditioned media in the presence of UTP (0.1 μM, 1 μM, 10 μM, 100 μM) or PBS control). (**A**) Genotype conditions utilized for Sholl analysis. (**B**) Representative traces of WT-WTACM and KON-KOACM neurons treated with PBS or 10 μM UTP. (**C**) Number of Sholl intersections at each radius from the neuronal soma, in WTN-WTACM and KON-KOACM conditions treated with PBS and 10 μM UTP. Significant main effects and interactions (*p* < 0.05) denoted by the following characters: * genotype; δ Sholl radius; Ɛ treatment; σ genotype x radius; ω genotype x treatment. **D-G.** UTP treatment (10–100 μM) increased the total number of Sholl intersections relative to PBS control in (**D**) WTN-WTACM (p ≤ 0.0115) and (**E**) KON-WTACM conditions (p ≤ 0.0281), but not in (**F**) WTN-KOACM or (**G**) KON-KOACM. Differences in overall branching levels between genotypes are shown in (**H**) PBS control (no significant differences), (**I**) KON-WTACM (p ≤ 0.0670) and (**J**) KON-KOACM (p ≤ 0.0172) in relation to WTN-WTACM. All data presented as means +/- SEM, with gray horizontal lines indicating control means. *n*=8; *n*=6 for 10 μM WTN-WTACM, KON-WTACM, KON-KOACM, and 1 μM WTN-KOACM. Significant differences between groups denoted by *; *p*<0.05

in response to exogenous UTP (Fig. 2E, I), as three of the four treatment concentrations exhibited elevated total Sholl intersections relative to PBS (0.1 μM UTP, $p = 0.0919$, $n = 8$; 1 μM UTP, $p = 0.0274$, $n = 8$; 10 μM UTP, $p = 0.0281$, $n = 6$; and 100 μM UTP, $p = 0.0484$, $n = 8$). However, neither WT neurons grown in *Fmr1* KO ACM with UTP (0.1 μM UTP, $p = 0.8677$, $n = 8$; 1 μM UTP, $p = 0.3251$, $n = 6$; 10 μM UTP, $p = 0.6017$, $n = 8$; 100 μM UTP, $p = 0.8266$, $n = 8$) nor *Fmr1* KO neurons in similar conditions (0.1 μM UTP $p = 0.2301$, $n = 8$; 1 μM UTP $p = 0.9989$, $n = 8$; 10 μM UTP $p > 0.9999$, $n = 6$; 100 μM UTP $p = 0.9222$, $n = 8$) demonstrated differences in the number of Sholl intersections relative to PBS ($n = 8$) (Fig. 2F, G, J).

P2Y$_2$ Receptor Expression is Decreased in *Fmr1* KO Neurons

Since UTP promotes neurite outgrowth and branching, we investigated the expression of P2Y receptors with high UTP affinity in WT and *Fmr1* KO primary cortical neurons. Notably, neuronal P2Y$_2$ receptor levels were significantly reduced in *Fmr1* KO cortical neurons relative to WT ($p = 0.0315$, $n = 6$, Fig. 3B). There were no other differences between WT and *Fmr1* KO neurons in the expression of other high affinity UTP receptors, including the P2Y$_1$ receptor ($p = 0.2119$, WT $n = 7$ and *Fmr1* KO $n = 8$, Fig. 3A), the P2Y$_4$ receptor ($p = 0.8484$, WT $n = 4$ and *Fmr1* KO $n = 3$, Fig. 3C), or the P2Y$_6$ receptor ($p = 0.7802$, $n = 5$, Fig. 3D).

Fmr1 KO Neuronal Activity is Significantly Elevated in Co-culture Conditions

Due to the significant influence of astrocyte secreted factors on neurite outgrowth during early development, we next examined how early modulation of outgrowth impacted the formation of neural connections in vitro, using astrocyte-neuron co-cultures plated on microelectrode arrays (MEAs). MEAs are electrophysiological preparations that permit the recording of a simplified neural circuit in vitro and were used to record neuronal firing activity 3x per week from 7 to 35 days of network development. Representative immunofluorescent images of co-cultures at 7DIV (Fig. 4A) demonstrate the close association between neurons and astrocytes, labelled with mitogen-associated protein 2 (MAP2) and glial fibrillary associated protein (GFAP), respectively. Definitions of the MEA parameters analyzed are presented in Table 1.

Mean firing rates of naïve vs. CNQX + AP-5-treated cells were not significantly different within either genotype culture condition at 7DIV, but by 10-12DIV, there was a visible decrease in the amount of activity detected from both WT and *Fmr1* KO CNQX + AP-5-treated cultures. In WT cultures, significant effects of treatment (Ɛ, $p < 0.0001$), time (δ, $p < 0.0001$), and treatment x time (ψ, $p < 0.0001$, Fig. 4D) were reported, as well as between treatment groups (7DIV versus 10DIV or 12DIV, both $p < 0.0001$). In *Fmr1* KO co-cultures, significant main effects of treatment (Ɛ, $p < 0.0001$), time (δ, $p = 0.0124$), and treatment x time (ψ, $p = 0.0412$, Fig. 4D) were also found, along with significant differences revealed by post-hoc comparisons at 10DIV and 12DIV (10DIV, $p = 0.0187$; and 12DIV, $p = 0.0008$).

Another important parameter to control was the overall health and firing capacity of each culture. To do this, we classified "active" electrodes within each MEA well as those recording > 5 spikes per minute throughout the duration of the experiment. Wells with at least 9/16 (> 50%) active electrodes at > 10DIV were retained for analysis of firing characteristics. Among these selected wells, an average of 12.68 of the 16 available electrodes per well consistently detected neuronal firing in WT co-cultures ($n = 13$ at 7DIV and $n = 6$ by 35DIV) once synaptic activity was established; versus 11.77 of 16 electrodes in *Fmr1* KO co-cultures ($p = 0.2115$, $n = 15$ at 7DIV and $n = 8$ by 35DIV, Fig. 4E). A significant effect of time was noted (δ; $p = 0.0040$), as the number of active electrodes was low during the earliest stages of recording, but rapidly stabilized as cultures developed functional networks.

To determine the general firing characteristics of WT vs. *Fmr1* KO neurons in co-culture, we compared their weighted mean firing rate, which measures the total number of neuronal spikes (i.e. putative action potentials) within the 10 min recording period normalized to the number of active electrodes. Within the first 14DIV, *Fmr1* KO neurons demonstrated a similar weighted mean firing rate in comparison to WTs (effects of genotype; $p = 0.0690$ and time δ; $p < 0.0001$), which was maintained as the cultures matured (effect of genotype; $p = 0.1644$; Fig. 4F). While weighted mean firing rate indicates the number of neuronal spikes, their temporal relation to each other can be measured using a synchrony index, with values close to 1 indicating a high degree of neuronal synchrony. Markedly, *Fmr1* KO firing synchrony was significantly reduced relative to WT throughout 35DIV, with significant effects of genotype (*, $p = 0.0247$, Fig. 4G) as well as time (δ, $p = 0.0363$).

Genotypic differences were also observed when we assessed the activity and connectivity of neurons measured at the level of single electrodes. Most strikingly, the frequency of neuronal bursting events was elevated in naïve *Fmr1* KO neuron-astrocyte co-culture relative to WT. A representative graphic of these bursting events is provided in Fig. 4C, which shows 30 s of bursting (blue lines) and network bursting (pink boxes) activity recorded by each electrode (single row) within a well of 16 MEA electrodes (16 rows shown in total). Neuronal burst frequency steadily
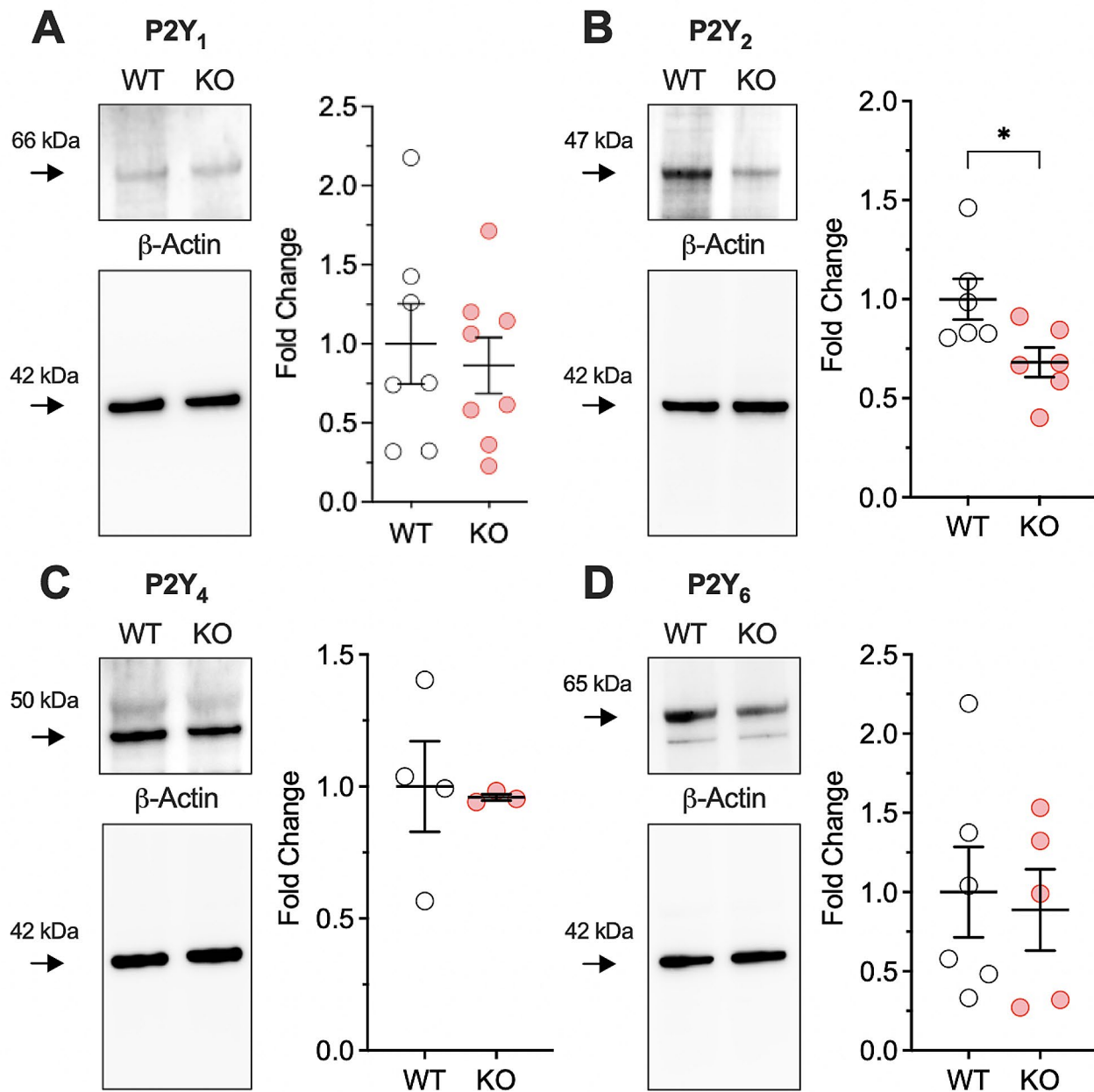
Fig. 3 Quantification of P2Y$_1$, P2Y$_2$, P2Y$_4$, and P2Y$_6$ excitatory purinergic receptors in neurons cultured from WT and *Fmr1* KO embryonic ($\sim$E16) cortex. Representative western blots and ß-actin loading controls are shown on each left panel, and neuron-associated receptor levels, expressed as fold change relative to WT means, are shown on each right panel. Expression of (**B**) neuronal P2Y$_2$ (47 kDa; $n=6$) was reduced in *Fmr1* KO cultures relative to WT ($p=0.0315$), while (**A**) P2Y$_1$ (66 kDa; WT $n=7$/*Fmr1* KO $n=8$), (**C**) P2Y$_4$ (50 kDa; WT $n=4$; *Fmr1* KO $n=3$), and (**D**) P2Y$_6$ (65 kDa; $n=5$) receptor expression did not differ between genotypes. All data presented as means +/- SEM. Significant differences between genotypes denoted by *; $p<0.05$

increased with culture maturation, and was visibly consistent between genotypes within the first two weeks in culture but diverged at 21DIV (Fig. 4H). We observed significant effects of genotype (*, $p=0.0064$) and time (δ, $p<0.0001$) on neuronal burst frequency throughout the 7-35DIV recording period, as well as a significant interaction of genotype x time (σ, $p=0.0091$). The number of neuronal spikes within each bursting event was significantly higher in WT versus *Fmr1* KO co-cultures during the earliest stages (7-21DIV) (effect of genotype *, $p=0.0071$, Fig. 4I left panel) but became remarkably consistent between genotypes at later time points. By 28DIV, *Fmr1* KO neuronal bursting events
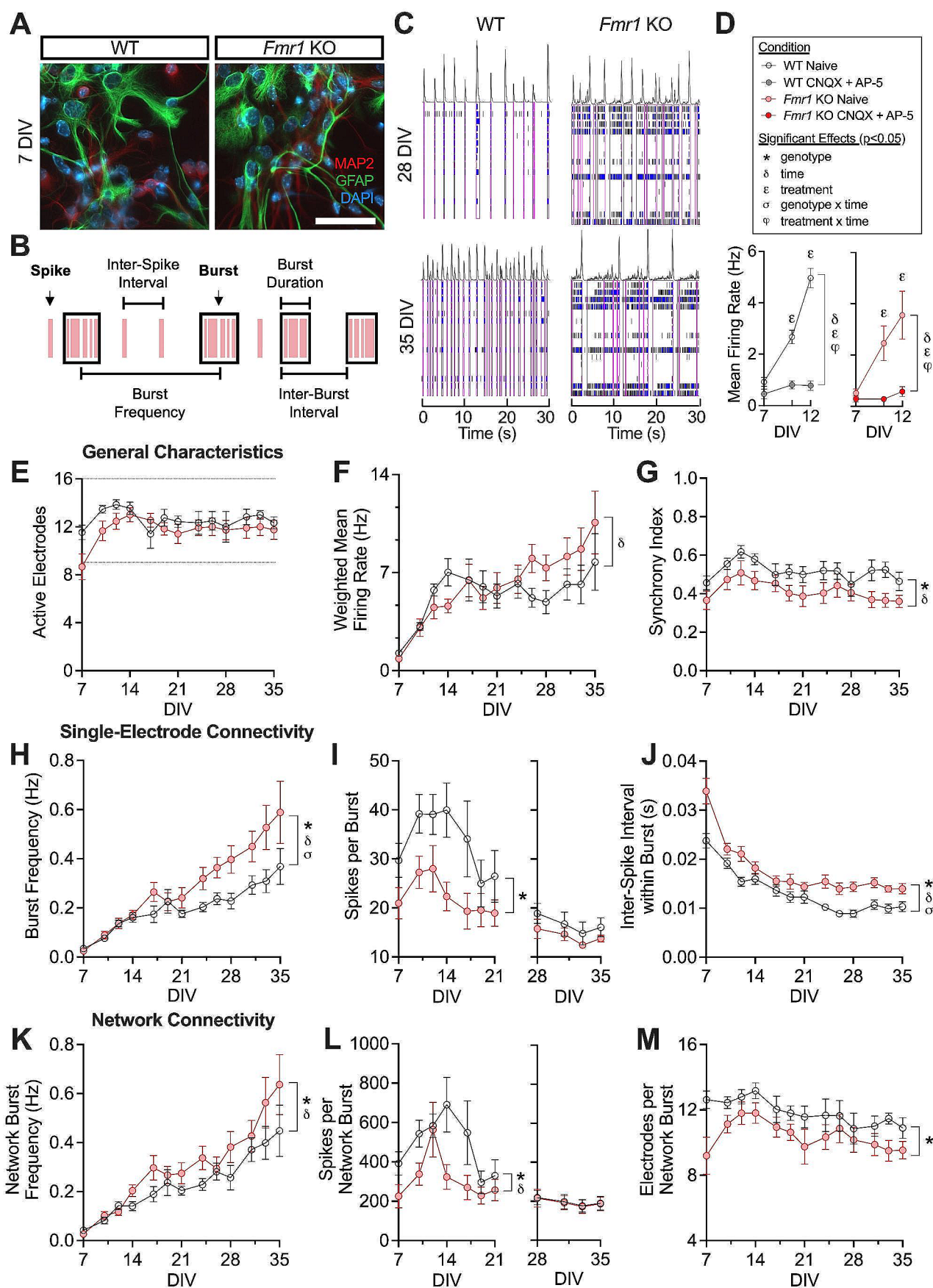
Fig. 4 Firing characteristics of WT and *Fmr1* KO co-cultured neurons between 7-35DIV. Neurons were co-cultured on microelectrode arrays (MEAs) with their respective genotype of astrocytes, then recorded 3x weekly (10 min/recording) from 7-35DIV. (**A**) Representative images of WT and *Fmr1* KO co-cultures at 7DIV, with neurons labelled in red (MAP2), astrocytes labelled in green (GFAP), and nuclei stained in blue (DAPI). Scale bar: 50 μm. (**B**) Schematic demonstrating MEA metrics measured at a single electrode, adapted from Axion Biosystems (2017). Spikes are shown as pink lines and bursts are shown as black boxes. (**C**) Representative raster plots of WT and *Fmr1* KO neuronal firing at 28DIV and 35DIV. Representative spikes from a single electrode are shown on the top row of each plot, and each subsequent row indicates the activity recorded at a single electrode over a 30 s recording period. Blue bars indicate neuronal bursts, and pink boxes indicate network bursts. (**D**) Mean firing rate of WT and *Fmr1* KO naïve (WT $n = 13$; *Fmr1* KO $n = 15$) and CNQX + AP-5-treated (WT $n = 15$; *Fmr1* KO $n = 12$) cultures. WT and *Fmr1* KO synaptic activity was effectively blocked by CNQX + AP-5 (10 μM) at 10DIV and 12DIV, but not 7DIV. **E-G.** General characteristics of WT ($n = 13$ at 7DIV; $n = 6$ by 35DIV) and *Fmr1* KO ($n = 15$ at 7DIV; $n = 8$ by 35DIV) neuronal activity. The number of active electrodes in analyzed wells (**E**) and weighted mean firing rate (**F**) did not differ between genotypes, but the synchronicity of *Fmr1* KO firing was reduced relative to WT ($p = 0.0247$) (**G**). **H-J.** Measurement of WT and *Fmr1* KO neuronal activity using single-electrode metrics of burst frequency ($p = 0.0064$) (**H**), spikes per burst ($p = 0.0071$) (**I**), and inter-spike interval within bursts ($p = 0.0002$) (**J**). Notably, *Fmr1* KO neurons demonstrated increased burst frequency relative to WT as the co-cultures matured (**H**). **K-M.** Comparison of WT vs. *Fmr1* KO neuronal activity using network-level metrics of network burst frequency ($p = 0.0241$) (**K**), number of spikes per network burst ($p = 0.0165$) (**L**), and the number of electrodes participating in network bursts ($p = 0.0296$) (**M**). Data points represent means +/- SEM. Main effects/interactions were considered significant at $p < 0.05$

contained the same number of spikes as their respective WT bursting events (28-35DIV, $p = 0.4506$, Fig. 4I right panel), indicating that the frequency of these coordinated firing events had increased in *Fmr1* KO co-cultured neurons. The average time between the spikes that comprise a bursting event, or the mean inter-spike interval within bursts, was significantly elevated in *Fmr1* KO cultures (Fig. 4J), with main effects of both genotype (*, $p = 0.0002$) and time (δ, $p < 0.0001$), as well as an interaction between genotype x time (σ, $p = 0.0447$).

In line with our observations of single-electrode bursts, the number of spikes per network burst was reduced in *Fmr1* KO cultures relative to WT during the first two weeks of recording (7-21DIV) ($p = 0.0165$, Fig. 4L left panel), then normalized by the end of the recording period (28-35DIV) ($p = 0.9730$; Fig. 4L right panel). The frequency of network bursts, shown with pink boxes in Fig. 4C, was increased in *Fmr1* KO co-culture in comparison to WT (Fig. 4K), with significant effects of both genotype (*, $p = 0.0241$) and time (δ, $p < 0.0001$). Reduced synchrony throughout the culture was also significantly reduced in *Fmr1* KO co-cultures versus WT (Fig. 4M) (*, main effect of genotype, $p = 0.0296$). This indicates that while *Fmr1* KO neurons in co-culture demonstrated greater levels of spontaneous

excitability compared to WTs, the excitatory firing between neurons within the *Fmr1* KO co-cultures were less organized and more asynchronous than that of WT neurons in WT conditions.

P2Y Antagonism Normalizes Aberrant *Fmr1* KO Neuronal Bursting

To determine whether elevated *Fmr1* KO astrocyte P2Y receptor levels [12] influenced burst and network burst frequency in our co-culture systems, we treated WT and *Fmr1* KO co-cultures with either the pan-P2Y antagonist suramin (0.1 μM) or the specific P2Y$_2$ antagonist AR-C 118925XX (1 μM and 10 μM) over the 7-35DIV recording period. Notably, treatment led to a robust decrease in the rapid firing of *Fmr1* KO neurons over time, which was evident when comparing burst frequency between naïve and AR-C 118925XX or suramin-treated cultures.

As seen in Fig. 5A, Fmr1 KO naïve ($n = 15$) and 1 μM AR-C 118925XX-treated ($n = 12$) co-cultures followed a similar burst frequency trajectory for the first 24DIV, then at 26DIV, AR-C-treated *Fmr1* KO neurons rapidly decreased bursting frequency, as AR-C appeared to normalize *Fmr1* KO neuron activity to WT naïve levels. Here, we observed significant main effects of treatment (ε, $p < 0.0001$), genotype (*, $p < 0.0001$), and time (δ, $p < 0.0001$) on burst frequency over the 7-35DIV period, as well as significant interactions between treatment x time (ψ, $p = 0.0005$), genotype x time (σ, $p = 0.0093$), and treatment x genotype (ω, $p = 0.0212$). The 1 μM and 10 μM AR-C 118925XX treatments were equivalent in their ability to decrease neuronal burst activity within a single genotype (WT 1 μM, $n = 14$, vs. WT 10 μM, $p = 0.7874$; *Fmr1* KO 1 μM, $n = 12$, vs. KO 10 μM, $n = 11$, $p = 0.6510$), so data from these treatments were pooled for group comparisons with naïve groups shown in Fig. 5B. A significant increase in burst frequency was observed in *Fmr1* KO naïve neurons relative to WT counterparts (*, $p = 0.0383$) at 28DIV, but this elevated burst frequency was normalized to WT levels following *Fmr1* KO AR-C 118925XX treatment (WT naïve vs. *Fmr1* KO AR-C 118925XX, $p = 0.9409$; Fmr1 KO naïve vs. *Fmr1* KO AR-C 118925XX, ε, $p = 0.0380$; Fig. 5B).

Similar to cultures treated with AR-C, in those treated with Suramin we observed significant main effects of treatment (ε; $p < 0.0001$), genotype (*; $p < 0.0001$), and time (δ; $p < 0.0001$) on neuronal burst frequency (Fig. 5H), as well as a significant interaction between genotype x time (σ; $p = 0.0149$). The burst frequency of *Fmr1* KO co-cultures ($n = 9$) appeared to be normalized to WT levels ($n = 10$) following suramin treatment after 1 month in vitro, with genotypic differences no longer present (Fig. 5I). As all treatments were done in parallel, the naïve groups acted as
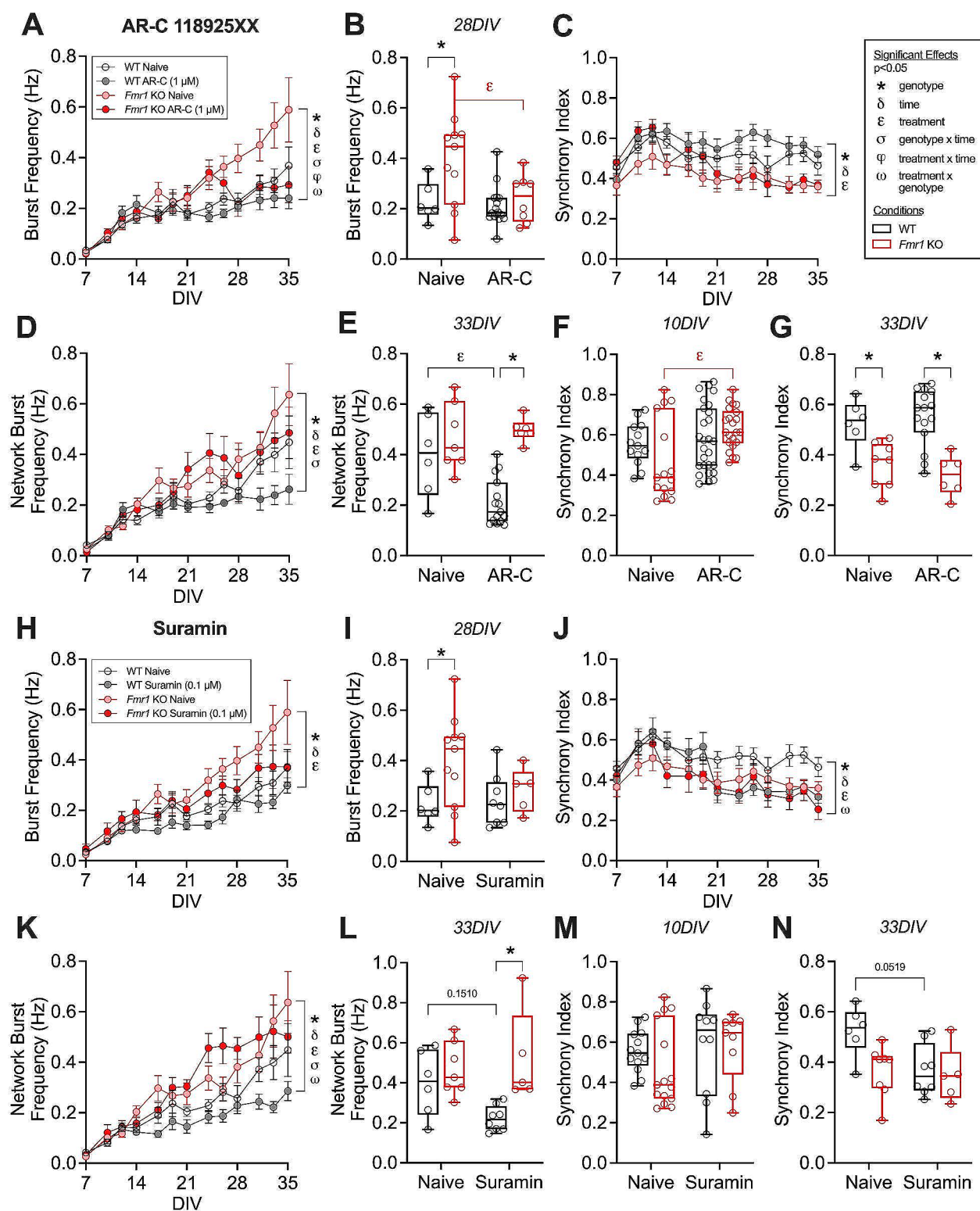
controls for each drug treatment and their values are shown in relative comparison to each treatment separately.

P2Y$_2$ antagonism also impacted the coordinated firing of neurons in network bursts, which was highly evident in

WT treatment groups, as WT AR-C treated neurons ($n=14$) had markedly decreased network burst frequency relative to WT naïve neurons ($n=13$) during the final recording week (Fig. 5D, E). Comparing network burst frequency in WT

Fig. 5 Normalization of aberrant neuronal *Fmr1* KO bursting and synchrony with P2Y antagonism. WT and *Fmr1* KO neurons were co-cultured on microelectrode arrays (MEAs) with their respective genotype of astrocytes, then treated 2x weekly with the selective P2Y$_2$ antagonist AR-C 118925XX (1 μM and 10 μM) or the pan-purinergic antagonist suramin (0.1 μM). Cultures were recorded 3x weekly (10 min/recording) from 7-35DIV. **A.** Single-electrode burst frequency following treatment with 1 μM AR-C 118925XX. Pooling both AR-C 118925XX treatment concentrations revealed a significant decrease in burst frequency at 28DIV ($p = 0.0383$) (**B**) that normalized *Fmr1* KO bursting to WT levels. **C.** Culture-wide synchrony index of 1 μM AR-C 118925XX-treated vs. naïve neurons. A transient elevation in *Fmr1* KO AR-C 118925XX (pooled) synchrony index was evident at 10DIV ($p = 0.0144$) (**F**) but was absent by 33DIV (**G**). **D.** Network burst frequency of naïve and AR-C 118925XX-treated neurons. A significant decrease in WT network burst frequency at 33DIV was observed following pooled AR-C 118925XX treatment ($p < 0.0001$) (**E**). **H.** Burst frequency of suramin-treated neurons, with further comparison showing that suramin did not significantly reduce *Fmr1* KO burst frequency at 28DIV (**I**). **J.** Synchrony index of naïve and suramin-treated neurons, with specific comparisons highlighted at 10DIV ($p = 0.0144$) (**M**) and 33DIV (**N**). **K.** Network burst frequency following suramin treatment, with further comparison showing a reduction in WT network burst frequency at 33DIV ($p = 0.0003$) (**L**). Naïve: WT $n = 13$ at 7DIV/$n = 6$ by 35DIV and *Fmr1* KO $n = 15$ at 7DIV/$n = 8$ by 35DIV. AR-C 118925XX 1 μM: WT $n = 14$ at 7DIV/$n = 8$ at 35DIV and *Fmr1* KO $n = 12$ at 7DIV/$n = 2$ at 35DIV; AR-C 118925XX 10 μM: WT $n = 13$ at 35DIV/$n = 7$ at 35DIV and *Fmr1* KO $n = 11$ at 35DIV/$n = 7$ at 35DIV. Suramin: WT $n = 10$ at 7DIV/$n = 8$ at 35DIV; *Fmr1* KO $n = 9$ at 7DIV/$n = 5$ at 35DIV. Data points on line graphs represent means +/-SEM. Box plots denote the interquartile range with whiskers extending to minimum and maximum values. Both main effects/interactions (line graphs) and post-hoc comparisons between treatments and genotypes (box plots) were considered significant at $p < 0.05$

and *Fmr1* KO naïve cultures with 1 μM AR-C 118925XX treated cultures, we observed significant main effects of treatment (ε, $p = 0.0109$), genotype (*, $p < 0.0001$), and time (δ, $p < 0.0001$), as well as a significant interaction between genotype x time (σ, $p < 0.0008$). By 33DIV, the network burst frequency of WT AR-C 118925XX-treated cultures was significantly reduced compared to WT naïve and *Fmr1* AR-C 118925XX-treated neurons ($p = 0.0061$ and $p < 0.0001$ respectively, Fig. 5E). While specific P2Y$_2$ antagonism decreased the frequency of bursts at a single electrode, it did not significantly alter *Fmr1* KO network burst frequency relative to that of the naïve group ($p = 0.6524$, Fig. 5E). With suramin treatment, network burst frequency differed between genotypes and treatments (Fig. 5K), with significant main effects of treatment (ε; $p = 0.0475$), genotype (*; $p < 0.0001$), and time (δ; $p < 0.0001$), as well as interactions between genotype x time (σ; $p < 0.0001$) and genotype x treatment (ω; $p = 0.0005$). We believe these results were largely due to decreased network bursting activity in suramin-treated WT cells. This reduced activity was particularly evident at 33DIV (Fig. 5L), where suramin treatment of WT co-cultures ($n = 8$) resulted in significantly lower network burst frequency than suramin-treated *Fmr1* KO neurons ($n = 5$; $p = 0.0120$).

P2Y Antagonism and Aberrant Synchronization of *Fmr1* KO Activity

The synchrony index of *Fmr1* KO co-cultures undergoing P2Y$_2$ antagonism was transiently normalized within the first ~2 weeks in vitro but returned to *Fmr1* KO naïve levels by ~24DIV (Fig. 5C). Significant main effects of treatment (ε; $p = 0.0019$), genotype (*; $p < 0.0001$), and time (δ; $p < 0.0001$) were noted when genotypes and treatment groups were compared over the full 7-35DIV period (Fig. 5C). A significant increase in the synchrony index was noted in *Fmr1* KO AR-C 118925XX-treated cultures relative to *Fmr1* KO naïve at 10DIV ($p = 0.0144$; Fig. 5F), but by 33DIV this difference was no longer present. Only genotypic differences in synchrony index were evident at 33DIV (WT vs. *Fmr1* KO AR-C treated, $p = 0.0003$; WT vs. *Fmr1* KO naïve, $p = 0.0161$; Fig. 5G).

In suramin-treated cultures, we also observed significant main effects of treatment (ε; $p = 0.0027$), genotype (*; $p < 0.0001$), and time (δ; $p < 0.0001$) on synchrony index (Fig. 5J), as well as a significant interaction between the two (ω; $p = 0.0423$). However, there was no effect of suramin treatment on WT or *Fmr1* KO synchrony relative to naïve at 10DIV ($p = 0.9820$ and $p = 0.6558$, respectively) or at 33DIV ($p = 0.0519$ and $p = 0.9821$, respectively).

High-dimensional Clustering of WT and *Fmr1* KO Co-culture Neural Activity

High-dimensional clustering with RSKC revealed unique subgroups within WT and *Fmr1* KO co-cultures at 28DIV. In total, 23 distinct MEA metrics were used from each co-culture condition (i.e. "features"; outlined in Table 1), and these features were used to partition samples of each genotype into clusters based on their similarities. At 28DIV, the WT samples formed 6 distinct clusters, and the *Fmr1* KOs formed 5 distinct clusters. Determination of distinct clustering of the two genotypic conditions and the features that defined the clusters was used to help highlight specific differences between synaptic behaviors of treatment groups not determined by specific comparisons of bursting presented in Figs. 4 and 5.

Over half of the WT naïve samples partitioned into Cluster 4, while other singles were found in Clusters 1, 3, and 6 (Fig. 6A, C). Co-cultures treated with ARC-118925XX and the pan P2Y antagonist suramin were often found clustered together, as seen in Clusters 2, 3, 5, and 6 (Fig. 6A, C). Samples treated with P2Y$_2$ antagonist ARC-118925XX had the least restricted pattern of activity across their features, as they were present in all 6 clusters (Fig. 6A, C). Among the 23 features (defined in Table 1) used to partition WT clusters, network burst frequency (NBF) was most

cluster-defining, as reflected by it having the largest average feature weight (mean weight = 0.388; Fig. 6B). The importance of NBF was also captured in the weighted t-SNE plot, as the clusters displayed similar activity on the t-SNE 1 axis as they did about the NBF variable (data not shown). Other features which highly influenced WT clustering included the number of electrodes participating in network bursts, weighted mean firing rate, synchrony index, and several single electrode-related parameters (Fig. 6B).

Relative to WT, the *Fmr1* KO co-cultures followed a very different activity profile. Suramin-treated *Fmr1* KO co-cultures displayed the narrowest activity profile, as they were found in only 2 of the 5 clusters (Fig. 6D, F). In comparison, naive and ARC-118925XX samples were each spread across 4 of the 5 clusters (Fig. 6D, F). Unlike the WT clusters, the *Fmr1* KO clusters reflected both treatment-specific and non-specific effects: Cluster 2 consisted solely of ARC-118925XX-treated samples and Cluster 3 consisted entirely of naïve samples, while Clusters 4 and 5 were heterogeneous (Fig. 6D, F). In forming these groups, RSKC determined that a synchrony-related metric (width at half height of normalized cross correlation, WAHHONCC) was the most useful feature (mean weight = 0.502; Fig. 6E). Specifically, the progression of *Fmr1* KO clusters about t-SNE 1 matches their progression across this metric (data not shown). The two additional synchrony-related features, namely synchrony index and area under normalized cross-correlation, were also highly involved in the partitioning of these RSKC clusters, along with differences in single and burst timing (NDIQR, NNDIQR) (Fig. 6E). Thus, P2Y antagonism elicited surprisingly different main effects on firing behaviors in *Fmr1* KO and WT cultures that were not detected in our pairwise analysis. Here, P2Y antagonism appeared to largely influence network bursting in WT conditions and synchronization of firing behavior in *Fmr1* KO conditions.

In addition to these key findings, this analysis also highlighted several other differences among the genotype conditions not included in the previous figures (Figs. 4 and 5). One noted genotypic difference was the number of factors within single-electrode and network connectivity categories that highly contributed to the groupings within the t-SNE plots. For WT conditions, there were 6 factors within the single-electrode connectivity category that contributed 20% or higher to cluster-defining compared to only two that matched that level of weighting in the *Fmr1* KO conditions. The same was true for parameters related to network connectivity, where two parameters had much higher contributions in WT cultures than others in the *Fmr1* KO conditions. In the *Fmr1* KO conditions, these parameters largely measured interval time parameters of either single burst or network activity, including the time between single burst events

Fig. 6 High-dimensional clustering of 28DIV WT and *Fmr1* KO MEA data using RSKC. A total of 23 measured MEA metrics, defined in Table 1, were used to cluster individual samples of each genotype. Pie charts show the proportion of WT (**A**) and *Fmr1* KO samples (**D**) that were assigned to each cluster by RSKC. Bar graphs constructed for each feature show their average RSKC weight across 100 iterations, with SEM error bars (**B**, **E**). The results of RSKC were input into the t-SNE algorithm to visualize high-dimensional relationships between WT samples (**C**) and *Fmr1* KO samples (**F**) in 2-dimensional space

(normalized duration interquartile range), the regularity of time between network bursts (network normalized duration of interquartile range and network burst-interval coefficient of variation) (Fig. 6E). In the WT conditions, contributing parameters were much more balanced and included measurements such as the number of bursting electrodes, time intervals between spikes and the number of spikes within a bursting event (Fig. 6B). Together, this suggests that alterations to firing activity in the *Fmr1* KO cultures are being largely driven by the frequency of spiking and bursting activity rather than global changes including the duration, activity or the magnitude of responses.

Discussion

Given the highly growing prevalence of ASDs and co-morbid conditions, there is an increasing demand for effective treatments regardless of syndrome etiology. Given the integral roles glial cells play in neurodevelopmental disorders, best treatment strategies need to also target both neuronal and glial aberrant activity in order to correct neurological function. Thus, purinergic signalling is an attractive candidate system given the widespread roles it plays in glial-neuronal function. This study highlights astrocyte-mediated signalling as a central element in the development of neuronal phenotypes and reveals that correction of dysfunctional purinergic signalling is sufficient to prevent aberrant FXS neuronal activity.

### Normal Neurite Outgrowth and Complexity is Enhanced by Purinergic Signalling

In early cortical development, neurons extend actin-rich growth cones that probe the CNS environment for cues in pathfinding [reviewed in 31, 32]. Rapid actin depolymerization and repolymerization cycles facilitate the addition of actin monomers to extend the axon [33]. Purinergic modulation of the actin-severing protein cofilin is known to elevate both neurite outgrowth and branching in vitro [34, 35]. In addition, P2Y receptors broadly activate the PI3K/Akt signalling pathway to influence axonal elongation [36–38]. In line with this, we observed that P2Y activation via exogenous UTP promoted neurite growth and arborization
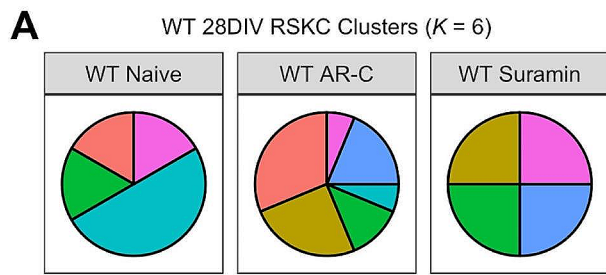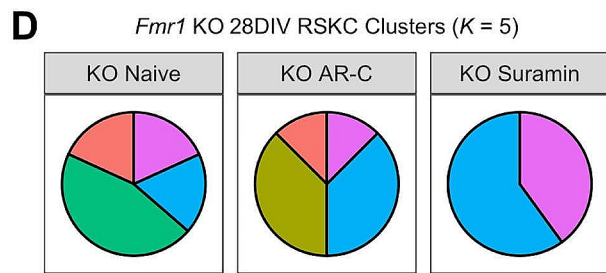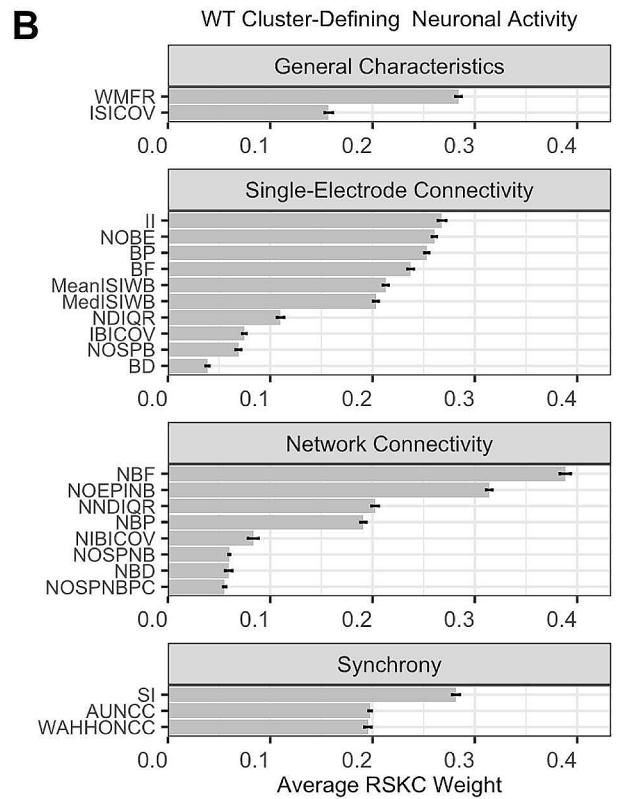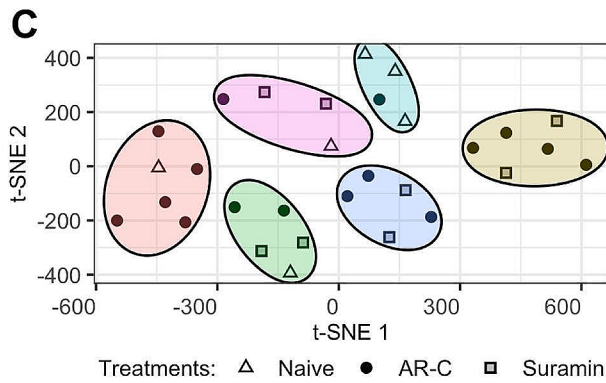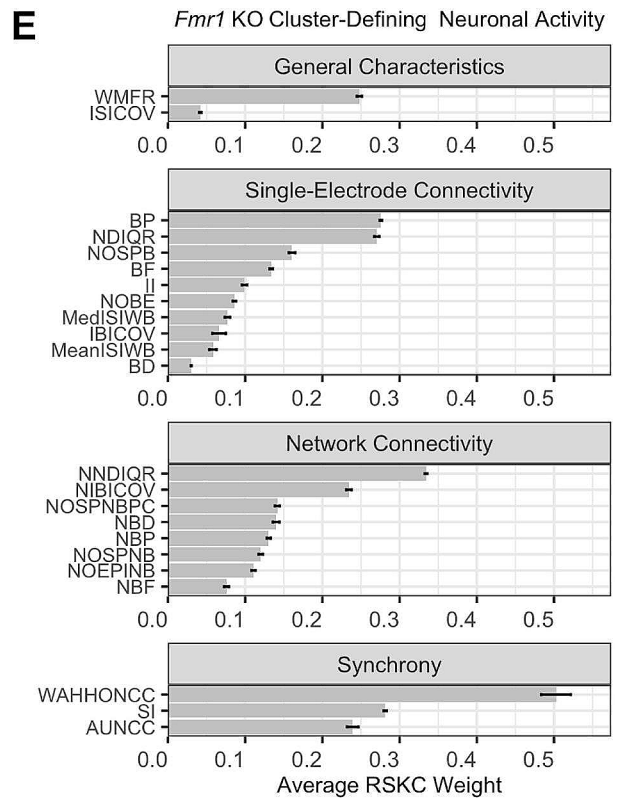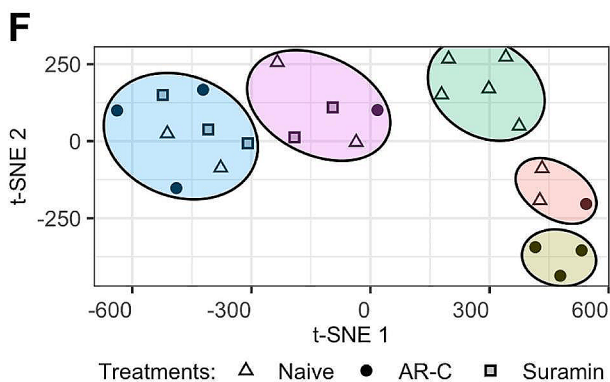
complexity of all neurons grown in WT ACM. Notably, the absence of FMRP in *Fmr1* KO neurons did not impair their capacity for purinergic-mediated growth, since unlike WT neurons, both the length and arborization of *Fmr1* KOs were significantly enhanced in response to low concentrations of UTP application. Neurite length of *Fmr1* KO neurons was also significantly greater than that of WT neurons when treated with high concentration UTP in WT ACM.

Given the enhanced sensitivity of *Fmr1* KO neurons to purinergic agonism in WT ACM, we compared *Fmr1* KO and WT neuronal expression of select purinergic receptors with affinity for UTP or its derivatives. Surprisingly, *Fmr1* KO neurons had a reduced level of $P2Y_2$ receptor expression in relation to WT neurons, but equivalent expression levels of $P2Y_1$, $P2Y_4$, and $P2Y_6$ receptors. Specifically, $P2Y_2$ activation alone has been shown to promote neurite outgrowth via phosphorylation of cofilin [34, 35], while $P2Y_4$ and $P2Y_6$ -mediated growth occurs primarily via the promotion of brain-derived neurotrophic factor signalling [39, 40]. Taken together, P2Y receptors can influence neurite outgrowth by a variety of mechanisms that may synergistically promote growth and arborization. Overall, the reduction of $P2Y_2$ in *Fmr1* KO neurons did not constrain the capacity for growth of these neurons in response to UTP and may represent attempted compensation by the neurons to prevent overactivation.

Abnormal *Fmr1* KO Neurite Outgrowth and Activity is Primarily Astrocyte-mediated

While UTP effectively increased neurite length and branching in WT ACM conditions, this was not the case with *Fmr1* KO ACM. In naïve conditions, both WT and *Fmr1* KO neurons treated with *Fmr1* KO soluble factors had significantly higher levels of outgrowth compared to those grown in WT ACM. Addition of exogenous UTP did not further promote growth of these cultures, suggesting that purine levels may already be elevated in *Fmr1* KO ACM. In line with this, P2Y receptor expression and activation on *Fmr1* KO cortical astrocytes is elevated in primary cultures [12] and P2Y activation leads to calcium mobilization and purine secretion [11, 41]. Notably, high concentrations of UTP treatment on neurons in WT ACM led to a similar degree of growth enhancement as *Fmr1* KO ACM did alone.

The influence of ACM on neurite outgrowth demonstrates the integral role of astrocyte signalling in early development. Although neuronal FMRP is expressed within dendrites and axonal growth cones [42] and has a role in axonal outgrowth and targeting [43, 44], we found that the absence of FMRP in cortical neurons was not sufficient to influence neurite extension. Our results were consistent with previous reports showing that WT hippocampal neurons assume a

Fmr1 KO-like morphology when grown in *Fmr1* KO ACM, and that astrocyte-specific silencing of *Fmr1* is sufficient to alter mouse motor neuron morphology and delay motor skill acquisition [9, 10]. Thus, therapeutic approaches targeting astrocyte signalling, rather than neuronal signalling, may be more effective at correcting aberrant neuronal morphology and connectivity in FXS.

In *Fmr1* KO co-cultures, cortical neurons demonstrated both increased burst frequency and increased network burst frequency by ~3 weeks *in vitro*. Enhanced activity followed a period of reduced firing, which is typically associated with periods of neurite elongation and synaptogenesis. This activity pattern is consistent with the development of hyperexcitable cortical circuits, such as the early transient period of hypoexcitability followed by elevated neuronal firing in the *Fmr1* KO rat visual cortex [45]. Studies using either FXS rodent models or iPSCs have also demonstrated neuronal hyperexcitability across MEA-measured networks [46–48] and localized interactions [49, 50] within the first two months of postnatal development. Importantly, deficits in neuronal firing reported for human FXS iPSC-derived neurons suggest that neuronal phenotypes across different brain regions and developmental stages are more variable in human populations [51].

Astrocytes regulate neuronal activity by the release of numerous factors critical to the development and maturation of synapses. An abundance of excitatory synaptic puncta and immature dendritic spines are present in FXS models [15, 16], while several astrocyte soluble factors that promote excitatory synaptogenesis, including hevin, interleukin-6, and thrombospondin-1 (TSP-1), are also elevated in *Fmr1* KO cortical astrocytes during the first several weeks of cortical development [12, 16, 21]. On the other hand, a lack of sufficient pruning and refinement of synapses can also lead to hyperactive connections. Approximately 50% of synapses are typically pruned following synaptogenesis to promote network efficiency and coordination [52]. Synaptic pruning is largely mediated via microglia and astrocytes through the activity of phagocytic receptors [53]. Several studies have demonstrated that the absence of postsynaptic FMRP is associated with pruning deficits [54, 55], suggesting that a blend of excess synaptogenesis and inadequate synaptic refinement leads to hyperexcitable bursting in *Fmr1* KO neurons (Fig. 7).

In addition to the number of synaptic connections, aberrant synaptic activity may also contribute to differences of excitable circuits observed in FXS. An imbalance of excitatory glutamatergic signalling paired with a lack of inhibitory GABAergic signalling is present in the *Fmr1* KO cortex [56, 57], and mediated at least in part by astrocytes. Astrocyte-specific conditional *Fmr1* KO mice display reduced cortical glutamate transporter-1 (GLT1) expression

Fig. 7 Potential mechanisms of action incited by elevated purinergic signalling in the *Fmr1* KO cortex include: (1) enhanced P2Y activation and intracellular Ca^{2+} levels in astrocytes; (2) increased release of synaptogenic factors (ex. TSP-1); (3) promotion of excitatory synaptic activity; (4) greater glial-mediated P2Y activation in adjacent astrocytes; and (5) elevated neuronal P2Y stimulation and PI3K/AKT-mediated axonal growth. Created with BioRender.com
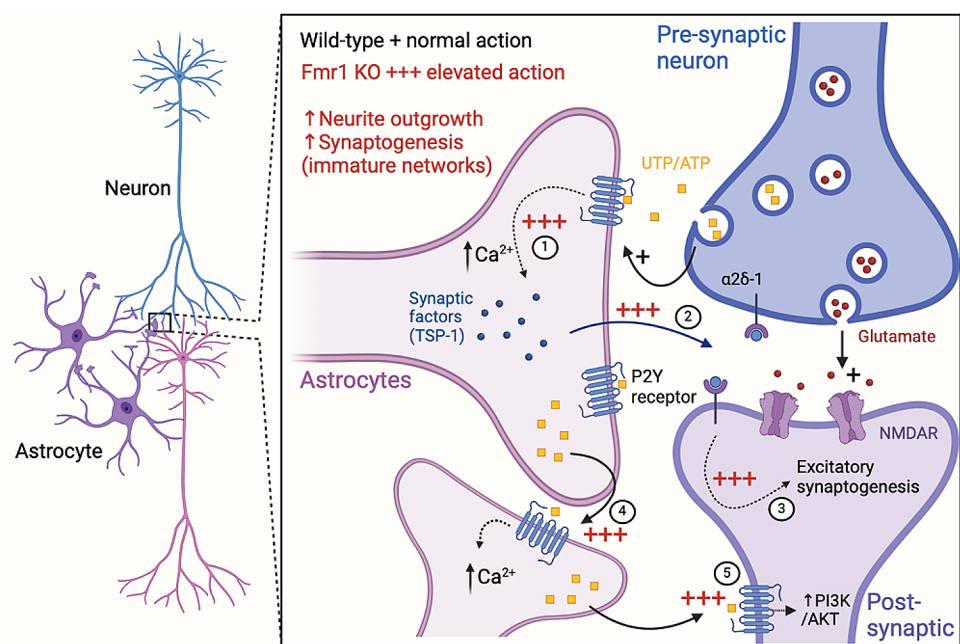
[58], which inhibits synaptic glutamate reuptake and leaves excess glutamate in the synaptic cleft. Correction of GLT1 expression rescued not only the resulting dendritic morphology but also normalized elevated excitatory signalling. Interestingly, pharmacological elevation of GLT1 transporters coupled with inhibition of ATP signalling is more effective at preventing seizures in rats than ATP or GLT1 modulation alone, suggesting converging functions of purinergic and glutamatergic signalling on epileptic activity [59].

Hyperexcitation of *Fmr1* KO Co-cultures is Modulated by Purinergic Dysregulation

Purinergic-driven activation of astrocytes prompts release of gliotransmitters including glutamate and ATP [41], pro-synaptic soluble factors (e.g. TSP-1) [12], and neuromodulators (e.g. Tenascin-C) [60]. Given this, it is not surprising that antagonism of P2Y receptors could help to normalize aberrant neuronal activity in *Fmr1* KO co-cultures. Antagonism via the specific P2Y$_2$ inhibitor ARC-118925XX prevented abnormal neuronal and network bursting activity, suggesting that P2Y$_2$ plays a significant role in mediating this activity in *Fmr1* KO co-cultures. Given that P2Y$_2$ expression is significantly higher in *Fmr1* KO astrocytes [12] but lower in neurons (Fig. 3) compared to WT, it is likely that antagonism to glial-mediated processes would occur to a greater extent and primarily underlie differences observed in neuronal activation. High-dimensional clustering analysis revealed many similarities between the neuronal activity of samples treated with AR-C 118925XX and suramin, which suggested these treatments were similarly effective at correcting aberrant activity. Notably, P2Y$_2$ receptor levels

are elevated in the brains of individuals with epilepsy, and increased levels of astrocyte P2Y$_2$ receptors are positively correlated with epileptiform activity [61, 62]. Increased burst and network burst frequencies during early development may indicate a predisposition toward seizure-like events as cortical networks mature, as seen in a subset of FXS patients [63]. Mitigation of ASD symptoms in adolescents treated with suramin also supports the role of purines in FXS or other ASDs [64], and together with our findings, suggests that purinergic receptors, particularly P2Y$_2$, are an effective target for future treatment approaches.

FXS is typically thought of as a disorder of overconnectivity and hypersynchrony, yet previous studies have reported both over- and underconnectivity across various brain regions, as well as both increased and decreased synchrony of firing [8, 49, 65–67]. For instance, overall neuronal connectivity in children with ASDs is transiently reduced relative to typically developing children, but is regionally elevated in the frontal cortex, indicating that connectivity is differentially regulated across brain regions and developmental stages [68]. Here, we observed a number of deficits in the synchronicity of *Fmr1* KO neuronal firing, both within local and culture-wide networks. At the level of a single electrode, the duration between spikes within a burst (i.e. inter-spike interval within bursts) was elevated in *Fmr1* KO cultures during time frames associated within increased burst frequency, indicating that while neurons in local networks engaged in more frequent bursts, their firing within those bursts was less tightly regulated. Overall firing across culture-wide networks was also less synchronous in *Fmr1* KO co-cultures than WTs, perhaps as a consequence of elevated single-electrode burst firing.

These discrepancies in connectivity and synchronicity may be understood by considering the role of inhibitory interneurons, which control the regularity of neuronal firing to promote the spread of synchronized excitation across a network [69]. In *Fmr1* KO mouse somatosensory cortical slices, GABAergic interneurons displayed reduced activity in response to glutamatergic agonism, and this lack of inhibitory input was found to impair the synchronicity of evoked excitatory neuronal firing [66]. Differences in spatial connectivity are also evident in the barrel cortex of FXS mice, with projection neurons of *Fmr1* KO mice less likely to establish functional synaptic connections than WT [70]. The lack of effect of P2Y antagonism on *Fmr1* KO synchrony index suggests that purinergic signalling plays a role in regulating the establishment and/or activity of neuronal connections, but not in coordinating them at the network level. Further research into the molecular mechanisms leading to the potential aberrant synchronization of neuronal activity during development could help correct fine-tuning circuitry in FXS and other ASDs.

Conclusions

Our current findings demonstrate that *Fmr1* KO astrocyte soluble factors, such as purines or pyrimidines, promote neurite elongation processes that initiate the formation of neural networks. Furthermore, neuronal hyperexcitation present in *Fmr1* KO cortical astrocyte-neuron co-cultures can be normalized with specific antagonism of P2Y$_2$ receptors. Future research targeting P2Y$_2$ antagonism in either astrocytes or neurons alone will help discern its cellular role in eliciting enhanced activity in the *Fmr1* KO cortex and its potential as a therapeutic target for FXS.

Author Contributions Kathryn Reynolds and Angela Scott wrote the main manuscript. Kathryn Reynolds prepared all figures. Kathryn Reynolds, Eileen Huang, Monica Sabbineni, Eliza Wiseman, Nadeem Murtaza, Matt Napier, Karun Singh, and Angela Scott were involved in data collection and experimental design contributing to Figs. 1, 2, 3, 4 and 5. Desmond Ahuja and Kathryn Murphy analyzed data and helped prepare Fig. 6. Angela Scott prepared Fig. 7. All authors reviewed the manuscript. Angela Scott received the grant for funding the project.

Data Availability No public datasets were generated or analysed during the current study.

Declarations

Ethics Approval All animal experimental protocols were authorized by the McMaster Animal Ethics Board (Animal Utilization Protocol 21-02-06), following Canadian Council on Animal Care policies.

Consent to Participate Not applicable.

Consent for Publication Not applicable.

Competing Interests The authors declare no competing interests.

References

1. Brown V, Jin P, Ceman S, Darnell JC, O'Donnell WT, Tenenbaum SA, Warren ST (2001) Microarray identification of FMRP-associated brain mRNAs and altered mRNA translational profiles in fragile X syndrome. Cell 107(4):477–487. https://doi.org/10.1016/S0092-8674(01)00568-2
2. Darnell JC, Van Driesche SJ, Zhang C, Hung KY, Mele A, Fraser CE, Darnell RB (2011) FMRP stalls ribosomal translocation on mRNAs linked to synaptic function and autism. Cell 146(2):247–261. https://doi.org/10.1016/j.cell.2011.06.013
3. Fu YH, Kuhl DP, Pizzuti A, Pieretti M, Sutcliffe JS, Richards S et al (1991) Variation of the CGG repeat at the fragile X site results in genetic instability: resolution of the Sherman paradox. Cell 67(6):1047–1058. https://doi.org/10.1016/0092-8674(91)90283-5
4. Pieretti M, Zhang FP, Fu YH, Warren ST, Oostra BA, Caskey CT, Nelson DL (1991) Absence of expression of the FMR-1 gene in fragile X syndrome. Cell 66(4):817–822. https://doi.org/10.1016/0092-8674(91)90125-i
5. Sutcliffe JS, Nelson DL, Zhang F, Pieretti M, Caskey CT, Saxe D, Warren ST (1992) DNA methylation represses FMR-1 transcription in fragile X syndrome. Hum Mol Genet 1(6):397–400. https://doi.org/10.1093/hmg/1.6.397
6. Verkerk AJMH, Pieretti M, Sutcliffe JS, Fu Y-H, Kuhl DPA, Pizzuti A, Warren ST (1991) Identification of a gene (FMR-1) containing a CGG repeat coincident with a breakpoint cluster region exhibiting length variation in fragile X syndrome. Cell 65(5):905–914. https://doi.org/10.1016/0092-8674(91)90397-H
7. Ethridge LE, White SP, Mosconi MW, Wang J, Byerly MJ, Sweeney JA (2016) Reduced habituation of auditory evoked potentials indicate cortical hyper-excitability in fragile X syndrome. Transl Psychiatry 6(4):e787. https://doi.org/10.1038/tp.2016.48
8. Ethridge LE, White SP, Mosconi MW, Wang J, Pedapati EV, Erickson CA, Sweeney JA (2017) Neural synchronization deficits linked to cortical hyper-excitability and auditory hypersensitivity in fragile X syndrome. Mol Autism 8(1):22. https://doi.org/10.1186/s13229-017-0140-1
9. Hodges JL, Yu X, Gilmore A, Bennett H, Tjia M, Perna JF, Zuo Y (2017) Astrocytic contributions to synaptic and learning abnormalities in a mouse model of fragile X syndrome. Biol Psychiatry 82(2):139–149. https://doi.org/10.1016/j.biopsych.2016.08.036
10. Jacobs S, Doering LC (2010) Astrocytes prevent abnormal neuronal development in the fragile X mouse. J Neurosci 30(12):4508–4514. https://doi.org/10.1523/jneurosci.5027-09.2010
11. Abbracchio MP, Burnstock G, Verkhratsky A, Zimmermann H (2009) Purinergic signalling in the nervous system: an overview. Trends Neurosci 32(1):19–29. https://doi.org/10.1016/j.tins.2008.10.001
12. Reynolds KE, Wong CR, Scott AL (2021) Astrocyte-mediated purinergic signaling is upregulated in a mouse model of Fragile

X syndrome. Glia 69(7):1816–1832. https://doi.org/10.1002/glia.23997

13. Eroglu C, Allen NJ, Susman MW, O'Rourke NA, Park CY, Ozkan E, Barres BA (2009) Gabapentin receptor alpha2delta-1 is a neuronal thrombospondin receptor responsible for excitatory CNS synaptogenesis. Cell 139(2):380–392. https://doi.org/10.1016/j.cell.2009.09.025

14. Tran MD, Neary JT (2006) Purinergic signaling induces thrombospondin-1 expression in astrocytes. Proc Natl Acad Sci USA 103(24):9321–9326. https://doi.org/10.1073/pnas.0603146103

15. Galvez R, Gopal AR, Greenough WT (2003) Somatosensory cortical barrel dendritic abnormalities in a mouse model of the fragile X mental retardation syndrome. Brain Res 971(1):83–89. https://doi.org/10.1016/s0006-8993(03)02363-1

16. Wallingford J, Scott AL, Rodrigues K, Doering LC (2017) Altered developmental expression of the astrocyte-secreted factors Hevin and SPARC in the fragile X mouse model. Front Mol Neurosci 10:268–268. https://doi.org/10.3389/fnmol.2017.00268

17. Brown MS, Singel D, Hepburn S, Rojas DC (2013) Increased glutamate concentration in the auditory cortex of persons with autism and first-degree relatives: a (1)H-MRS study. Autism Res 6(1):1–10. https://doi.org/10.1002/aur.1260

18. Gibson JR, Bartley AF, Hays SA, Huber KM (2008) Imbalance of neocortical excitation and inhibition and altered UP states reflect network hyperexcitability in the mouse model of fragile X syndrome. J Neurophysiol 100(5):2615–2626. https://doi.org/10.1152/jn.90752.2008

19. Jacobs S, Doering LC (2009) Primary dissociated astrocyte and neuron co-culture. In L. C. Doering (Ed.), *Protocols for Neural Cell Culture* (Fourth Edition ed., pp. 269–284). New York, NY: Humana

20. Cheng C, Lau SKM, Doering LC (2016) Astrocyte-secreted thrombospondin-1 modulates synapse and spine defects in the fragile X mouse model. Mol Brain 9(1):74. https://doi.org/10.1186/s13041-016-0256-9

21. Krasovska V, Doering LC (2018) Regulation of IL-6 secretion by astrocytes via TLR4 in the fragile X mouse model. Front Mol Neurosci 11:272–272. https://doi.org/10.3389/fnmol.2018.00272

22. Cui JD, Xu ML, Liu EYL, Dong TTX, Lin HQ, Tsim KWK, Bi CWC (2016) Expression of globular form acetylcholinesterase is not altered in P2Y1R knock-out mouse brain. Chem Biol Interact 259(Pt B):291–294. https://doi.org/10.1016/j.cbi.2016.06.028

23. D'Ambrosi N, Iafrate M, Saba E, Rosa P, Volonté C (2007) Comparative analysis of P2Y4 and P2Y6 receptor architecture in native and transfected neuronal systems. Biochim et Biophys Acta (BBA) - Biomembr 1768(6):1592–1599. https://doi.org/10.1016/j.bbamem.2007.03.020

24. Sage CL, Marcus DC (2002) Immunolocalization of P2Y4 and P2Y2 purinergic receptors in strial marginal cells and vestibular dark cells. J Membr Biol 185(2):103–115. https://doi.org/10.1007/s00232-001-0116-z

25. Koizumi S, Shigemoto-Mogami Y, Nasu-Tada K, Shinozaki Y, Ohsawa K, Tsuda M, Inoue K (2007) UDP acting at P2Y6 receptors is a mediator of microglial phagocytosis. Nature 446(7139):1091–1095. https://doi.org/10.1038/nature05704

26. Kondo Y, Salibian-Barrera M, Zamar R (2016) RSKC: an R package for a robust and sparse K-means clustering algorithm. J Stat Softw 72(5):1–26. https://doi.org/10.18637/jss.v072.i05

27. Balsor JL, Arbabi K, Singh D, Kwan R, Zaslavsky J, Jeyanesan E, Murphy KM (2021) A practical guide to sparse K-means clustering for studying molecular development of the human brain. Front Neurosci 15:668293. https://doi.org/10.3389/fnins.2021.668293

28. Van der Maaten L, Hinton G (2008) Visualizing data using t-SNE. J Mach Learn Res 9(11)

29. Kobak D, Berens P (2019) The art of using t-SNE for single-cell transcriptomics. Nat Commun 10(1):5416. https://doi.org/10.1038/s41467-019-13056-x

30. Wattenberg M, Viégas FB, Johnson I (2016) *How to Use t-SNE Effectively*

31. Dent EW, Gupton SL, Gertler FB (2011) The growth cone cytoskeleton in axon outgrowth and guidance. Cold Spring Harb Perspect Biol 3(3). https://doi.org/10.1101/cshperspect.a001800

32. Gillespie LN (2003) Regulation of axonal growth and guidance by the neurotrophin family of neurotrophic factors. Clin Exp Pharmacol Physiol 30(10):724–733. https://doi.org/10.1046/j.1440-1681.2003.03909.x

33. Marsick BM, Flynn KC, Santiago-Medina M, Bamburg JR, Letourneau PC (2010) Activation of ADF/cofilin mediates attractive growth cone turning toward nerve growth factor and netrin-1. Dev Neurobiol 70(8):565–588. https://doi.org/10.1002/dneu.20800

34. Peterson TS, Thebeau CN, Ajit D, Camden JM, Woods LT, Wood WG, Weisman GA (2013) Up-regulation and activation of the P2Y(2) nucleotide receptor mediate neurite extension in IL-1β-treated mouse primary cortical neurons. J Neurochem 125(6):885–896. https://doi.org/10.1111/jnc.12252

35. Pooler AM, Guez DH, Benedictus R, Wurtman WJ (2005) Uridine enhances neurite outgrowth in nerve growth factor-differentiated pheochromocytoma cells. Neuroscience 134:207–214

36. Heine C, Sygnecka K, Scherf N, Grohmann M, Bräsigk A, Franke H (2015) P2Y1 receptor mediated neuronal fibre outgrowth in organotypic brain slice co-cultures. Neuropharmacology 93:252–266. https://doi.org/10.1016/j.neuropharm.2015.02.001

37. Sanchez S, Sayas CL, Lim F, Diaz-Nido J, Avila J, Wandosell F (2001) The inhibition of phosphatidylinositol-3-kinase induces neurite retraction and activates GSK3. J Neurochem 78(3):468–481. https://doi.org/10.1046/j.1471-4159.2001.00453.x

38. Van Kolen K, Slegers H (2006) Integration of P2Y receptor-activated signal transduction pathways in G protein-dependent signalling networks. Purinergic Signalling 2(3):451–469. https://doi.org/10.1007/s11302-006-9008-0

39. Finkbeiner S (2000) Calcium regulation of the brain-derived neurotrophic factor gene. Cell Mol Life Sci 57(3):394–401. https://doi.org/10.1007/pl00000701

40. Rabacchi SA, Kruk B, Hamilton J, Carney C, Hoffman JR, Meyer SL, Baird DH (1999) BDNF and NT4/5 promote survival and neurite outgrowth of pontocerebellar mossy fiber neurons. J Neurobiol 40(2):254–269

41. Scemes E, Giaume C (2006) Astrocyte calcium waves: what they are and what they do. Glia 54(7):716–725. https://doi.org/10.1002/glia.20374

42. Antar LN, Dictenberg JB, Plociniak M, Afroz R, Bassell GJ (2005) Localization of FMRP-associated mRNA granules and requirement of microtubules for activity-dependent trafficking in hippocampal neurons. Genes Brain Behav 4(6):350–359. https://doi.org/10.1111/j.1601-183X.2005.00128.x

43. Morales J, Hiesinger PR, Schroeder AJ, Kume K, Verstreken P, Jackson FR, Hassan BA (2002) Drosophila fragile X protein, DFXR, regulates neuronal morphology and function in the brain. Neuron 34(6):961–972. https://doi.org/10.1016/S0896-6273(02)00731-6

44. Pan L, Zhang YQ, Woodruff E, Broadie K (2004) The drosophila fragile X gene negatively regulates neuronal elaboration and synaptic differentiation. Curr Biol 14(20):1863–1870. https://doi.org/10.1016/j.cub.2004.09.085

45. Berzhanskaya J, Phillips MA, Shen J, Colonnese MT (2016) Sensory hypo-excitability in a rat model of fetal development in fragile X syndrome. Sci Rep 6:30769. https://doi.org/10.1038/srep30769

46. Graef JD, Wu H, Ng C, Sun C, Villegas V, Qadir D, Wallace O (2020) Partial FMRP expression is sufficient to normalize neuronal hyperactivity in fragile X neurons. Eur J Neurosci 51(10):2143–2157. https://doi.org/10.1111/ejn.14660

47. Liu XS, Wu H, Krzisch M, Wu X, Graef J, Muffat J, Jaenisch R (2018) Rescue of fragile X syndrome neurons by DNA methylation editing of the FMR1 gene. Cell 172(5):979–992e976. https://doi.org/10.1016/j.cell.2018.01.012

48. Moskalyuk A, Van De Vijver S, Verstraelen P, De Vos WH, Kooy RF, Giugliano M (2019) Single-cell and neuronal network alterations in an in vitro model of fragile X syndrome. Cereb Cortex 30(1):31–46. https://doi.org/10.1093/cercor/bhz068

49. Gonçalves JT, Anstey JE, Golshani P, Portera-Cailliau C (2013) Circuit level defects in the developing neocortex of fragile X mice. Nat Neurosci 16(7):903–909. https://doi.org/10.1038/nn.3415

50. Zhang Y, Bonnan A, Bony G, Ferezou I, Pietropaolo S, Ginger M, Frick A (2014) Dendritic channelopathies contribute to neocortical and sensory hyperexcitability in Fmr1(-/y) mice. Nat Neurosci 17(12):1701–1709. https://doi.org/10.1038/nn.386

51. Telias M, Kuznitsov-Yanovsky L, Segal M, Ben-Yosef D (2015) Functional deficiencies in fragile X neurons derived from human embryonic stem cells. J Neurosci 35(46):15295–15306. https://doi.org/10.1523/jneurosci.0317-15.2015

52. Lossi L, Merighi A (2003) In vivo cellular and molecular mechanisms of neuronal apoptosis in the mammalian CNS. Prog Neurobiol 69(5):287–312. https://doi.org/10.1016/s0301-0082(03)00051-0

53. Chung WS, Clarke LE, Wang GX, Stafford BK, Sher A, Chakraborty C, Barres BA (2013) Astrocytes mediate synapse elimination through MEGF10 and MERTK pathways. Nature 504(7480):394–400. https://doi.org/10.1038/nature12776

54. Bagni C, Greenough WT (2005) From mRNP trafficking to spine dysmorphogenesis: the roots of fragile X syndrome. Nat Rev Neurosci 6(5):376–387. https://doi.org/10.1038/nrn1667

55. Patel AB, Loerwald KW, Huber KM, Gibson JR (2014) Post-synaptic FMRP promotes the pruning of cell-to-cell connections among pyramidal neurons in the L5A neocortical network. J Neurosci 34(9):3413–3418. https://doi.org/10.1523/jneurosci.2921-13.2014

56. El Idrissi A, Ding XH, Scalia J, Trenkner E, Brown WT, Dobkin C (2005) Decreased GABA(A) receptor expression in the seizure-prone fragile X mouse. Neurosci Lett 377(3):141–146. https://doi.org/10.1016/j.neulet.2004.11.087

57. Fatemi SH, Folsom TD (2011) Dysregulation of fragile X mental retardation protein and metabotropic glutamate receptor 5 in superior frontal cortex of individuals with autism: a postmortem brain study. Mol Autism 2(1):6. https://doi.org/10.1186/2040-2392-2-6

58. Higashimori H, Schin CS, Chiang MS, Morel L, Shoneye TA, Nelson DL, Yang Y (2016) Selective deletion of astroglial FMRP dysregulates glutamate transporter GLT1 and contributes to fragile X syndrome phenotypes in vivo. J Neurosci 36(27):7079–7094. https://doi.org/10.1523/jneurosci.1069-16.2016

59. Soni N, Koushal P, Reddy BV, Deshmukh R, Kumar P (2015) Effect of GLT-1 modulator and P2X7 antagonists alone and in combination in the kindling model of epilepsy in rats. Epilepsy Behav 48:4–14. https://doi.org/10.1016/j.yebeh.2015.04.056

60. Reynolds KE, Krasovska V, Scott AL (2021) Converging purinergic and immune signaling pathways drive IL-6 secretion by fragile X cortical astrocytes via STAT3. J Neuroimmunol 361:577745. https://doi.org/10.1016/j.jneuroim.2021.577745

61. Alves M, Gomez-Villafuertes R, Delanty N, Farrell MA, O'Brien DF, Miras-Portugal MT, Engel T (2017) Expression and function of the metabotropic purinergic P2Y receptor family in experimental seizure models and patients with drug-refractory epilepsy. Epilepsia 58(9):1603–1614. https://doi.org/10.1111/epi.13850

62. Sukigara S, Dai H, Nabatame S, Otsuki T, Hanai S, Honda R, Itoh M (2014) Expression of astrocyte-related receptors in cortical dysplasia with intractable epilepsy. J Neuropathol Exp Neurol 73(8):798–806. https://doi.org/10.1097/nen.0000000000000099

63. Musumeci SA, Hagerman RJ, Ferri R, Bosco P, Bernardina BD, Tassinari CA, Elia M (1999) Epilepsy and EEG findings in males with fragile X syndrome. Epilepsia 40(8):1092–1099. https://doi.org/10.1111/j.1528-1157.1999.tb00824.x

64. Naviaux RK, Curtis B, Li K, Naviaux JC, Bright AT, Reiner GE, Townsend J (2017) Low-dose suramin in autism spectrum disorder: a small, phase I/II, randomized clinical trial. Ann Clin Transl Neurol 4(7):491–505. https://doi.org/10.1002/acn3.424

65. Müller R-A, Shih P, Keehn B, Deyoe JR, Leyden KM, Shukla DK (2011) Underconnected, but how? A survey of functional connectivity MRI studies in autism spectrum disorders. Cereb Cortex 21(10):2233–2243. https://doi.org/10.1093/cercor/bhq296

66. Paluszkiewicz SM, Olmos-Serrano JL, Corbin JG, Huntsman MM (2011) Impaired inhibitory control of cortical synchronization in fragile X syndrome. J Neurophysiol 106(5):2264–2272. https://doi.org/10.1152/jn.00421.2011

67. Testa-Silva G, Loebel A, Giugliano M, de Kock CP, Mansvelder HD, Meredith RM (2012) Hyperconnectivity and slow synapses during early development of medial prefrontal cortex in a mouse model for mental retardation and autism. Cereb Cortex 22(6):1333–1342. https://doi.org/10.1093/cercor/bhr224

68. Dajani DR, Uddin LQ (2016) Local brain connectivity across development in autism spectrum disorder: a cross-sectional investigation. Autism Res 9(1):43–54. https://doi.org/10.1002/aur.1494

69. Rio C-D, C. A., Huntsman MM (2014) The contribution of inhibitory interneurons to circuit dysfunction in Fragile X Syndrome. Front Cell Neurosci 8(245). https://doi.org/10.3389/fncel.2014.00245

70. Bureau I, Shepherd GMG, Svoboda K (2008) Circuit and plasticity defects in the developing somatosensory cortex of Fmr1 knock-out mice. J Neurosci 28(20):5178–5188. https://doi.org/10.1523/jneurosci.1076-08.2008